

Accepted Manuscript

A vertex centred Finite Volume Jameson–Schmidt–Turkel (JST) algorithm for a mixed conservation formulation in solid dynamics

Miquel Aguirre, Antonio J. Gil, Javier Bonet, Aurelio Arranz Carreño

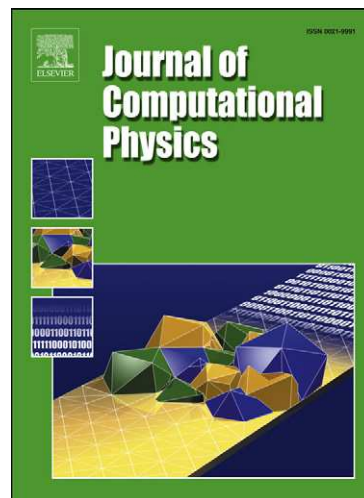
PII: S0021-9991(13)00811-5
DOI: [10.1016/j.jcp.2013.12.012](http://dx.doi.org/10.1016/j.jcp.2013.12.012)
Reference: YJCPH 4974

To appear in: *Journal of Computational Physics*

Received date: 5 July 2013
Revised date: 19 November 2013
Accepted date: 5 December 2013

Please cite this article in press as: M. Aguirre et al., A vertex centred Finite Volume Jameson–Schmidt–Turkel (JST) algorithm for a mixed conservation formulation in solid dynamics, *Journal of Computational Physics* (2013), <http://dx.doi.org/10.1016/j.jcp.2013.12.012>

This is a PDF file of an unedited manuscript that has been accepted for publication. As a service to our customers we are providing this early version of the manuscript. The manuscript will undergo copyediting, typesetting, and review of the resulting proof before it is published in its final form. Please note that during the production process errors may be discovered which could affect the content, and all legal disclaimers that apply to the journal pertain.



A vertex centred Finite Volume Jameson-Schmidt-Turkel (JST) algorithm for a mixed conservation formulation in solid dynamics

Miquel Aguirre, Antonio J. Gil, Javier Bonet, Aurelio Arranz Carreño

*Civil and Computational Engineering Centre, College of Engineering
Swansea University, Singleton Park, SA2 8PP, United Kingdom*

Abstract

A vertex centred Finite Volume algorithm is presented for the numerical simulation of fast transient dynamics problems involving large deformations. A mixed formulation based upon the use of the linear momentum, the deformation gradient tensor and the total energy as conservation variables is discretised in space using linear triangles and tetrahedra in two-dimensional and three-dimensional computations, respectively. The scheme is implemented using central differences for the evaluation of the interface fluxes in conjunction with the Jameson-Schmidt-Turkel (JST) artificial dissipation term. The discretisation in time is performed by using a Total Variational Diminishing (TVD) two-stage Runge-Kutta time integrator. The JST algorithm is adapted in order to ensure the preservation of linear and angular momenta. The framework results in a low order computationally efficient solver for solid dynamics, which proves to be very competitive in nearly incompressible scenarios and bending dominated applications.

Keywords: Fast dynamics, mixed formulation, conservation laws, Mie-Gruneisen, Finite Volume Method, vertex centred, Jameson-Schmidt-Turkel

1. Introduction

A new Lagrangian mixed formulation [1–4] has been recently developed for the simulation of fast transient dynamics problems. The methodology is presented in the form of a system of first order conservation laws where the linear momentum and the deformation gradient tensor are regarded as the

two main conservation variables. An additional conservation equation can also be formulated for the total energy of the system which, in the case of reversible elastodynamics, decouples from the rest of the conservation equations. The use of physical equations written in the form of conservation laws enables the use of traditional Computational Fluid Dynamics (CFD) discretisations within the solid dynamics context and, ultimately, an implementation into a Finite Volume framework.

Early attempts at applying the Finite Volume Method (FVM) in the context of solid dynamics date to references [5–9], using displacement based formulations for linear elasticity. Eulerian Finite Volume Godunov methods, classically used for modelling compressible gas dynamics, have been also adapted to model plastic flows in solid dynamics [10–13]. Subsequently, and perhaps more significantly to the current paper, this work was adapted to a Lagrangian framework by several authors [13–15]. Specifically, in [14], a Lagrangian Godunov method was presented for hyperelastic materials.

In contrast to displacement based formulations, references [1–3] have demonstrated that the same order of accuracy can be obtained for both strains (or stresses) and velocities (or displacements once integrated in time) if the new mixed formulation is employed. This formulation enables the use of low order elements without exhibiting volumetric locking in nearly incompressible situations [16] and, therefore, it is proposed as an alternative to nodal Finite Element formulations [17–27].

The use of low order elements is regarded as very advantageous in solid dynamics due to its lower computational cost (usually related to the evaluation of the constitutive model) and simplicity in the simulation of contact problems. Furthermore, by using CFD discretisations, a large wealth of shock capturing techniques becomes available. In reference [1], the proposed formulation was implemented using a two-dimensional Finite Volume cell centred upwind technique, where Riemann Solvers use the wave characteristics information in order to advance the solution in time (see for example references [28–30]). The solution was obtained with second order accuracy by using linear reconstruction and limiters, which preserve the solution monotonicity in the vicinity of sharp gradients.

In reference [3], the authors present an alternative two-dimensional implementation of the mixed formulation in the form a Two-Stage Taylor-Galerkin algorithm, where results are compared against those of [1] for a series of benchmark examples. Reference [2] introduces a new Petrov Galerkin (PG) Finite Element Method [31] as an alternative form of stabilisation for the

set of mixed conservation equations. Moreover, in the same work [2] the stabilised spatial discretisation is also re-written in the form of the Variational Multiscale Method (VMS) initially introduced in [32]. Both references [2, 3] provide two- and three-dimensional results where velocities and strains (stresses) converge at the same rate with excellent behaviour in bending dominated scenarios. Finally, since the formulation is written in the form of a system of conservation laws, it is very suitable for spatial discretisation using Discontinuous Galerkin Methods, such as in reference [4] where the Hybridizable Discontinuous Galerkin (HDG) version is preferred.

The current paper introduces an alternative two- and three-dimensional implementation within the vertex centred Finite Volume context, which provides a general low cost framework for large scale problems. To do so, the well known Jameson-Schmidt-Turkel (JST) scheme [33] is used. The scheme was first introduced in reference [33] for the solution of the Euler equations for rectangular structured meshes, and later extended to unstructured meshes in references [34–37]. The scheme uses a central differences approach, equivalent to a Galerkin Finite Element discretisation with linear elements [34, 38–41] plus a blend of a non divided Laplacian and a biharmonic operator in order to add artificial diffusion [33–35, 42–45].

The attractiveness of this scheme relies mainly on computational cost aspects. First of all, it is a nodal based Finite Volume scheme and therefore, the number of evaluations of the stress tensor (constitutive model) is reduced drastically as compared to a cell centred scheme since, as stated in [45, 46], the number of elements is from 5 to 7 times the number of nodes in a tetrahedral mesh. Secondly, the computational effort when computing the flux gradients is reduced by half in a vertex centred scheme since the loops are performed on edges instead of faces (as in a cell centred scheme), being the ratio between the number of faces and the number of edges of around 2 to 1 [46]. Furthermore, the combination of the artificial dissipation term and the shock capturing switch gives a second order monotonicity preserving algorithm without the use of linear reconstruction and slope limiters. Finally, since the JST scheme is present in a large amount of available CFD software [47, 48], its implementation into a solid dynamics framework can ease the adaptation of existing codes. Nevertheless, it is well known that the JST scheme suffers from excessive dissipative solutions [39] since it does not use wave information to advance the solution in time. Therefore, mesh refinements have to be performed in order to obtain accuracies comparable to those of other methodologies (such as PG or upwind FVM with linear

reconstruction).

The current paper aims to establish a robust framework for adapting the JST formulation to solid dynamics. In order to adapt the original JST scheme to the problem at hand, dissipation will only be added to the linear momentum equation. The update of the deformation gradient tensor will be left as a numerical gradient of the velocities with the use of no additional dissipation. This will enable the discrete satisfaction of the compatibility conditions of the deformation mapping (i.e. curl-free)[1, 3]. Special attention must be paid to the numerical quadrature of the boundary fluxes through the use of a weighted nodal flux average carried out at the boundary faces. The spatial discretisation will be combined with a two-stage Total Variation Diminishing (TVD) Runge-Kutta time integrator [49]. The displacements are integrated in time using a trapezoidal rule which is combined with a Lagrange multiplier minimisation procedure to ensure the conservation of angular momentum. An additional correction of the numerical dissipation to ensure the conservation of the linear momentum, whilst preserving the accuracy order, is also presented.

In the following sections, the implementation of the method will be explained. Section 2 will introduce the general governing equations of the problem. Section 3 will summarise the JST spatial discretisation scheme and explain its adaptation to the solid dynamics framework. Section 4 introduces the Runge-Kutta time integrator used for the problem variables and the trapezoidal rule employed for the advancement of the displacements in time. Section 5 explains the numerical corrections introduced in order to satisfy conservation of linear and angular momentum. Section 6 summarises the solution procedure. In section 7 a set of numerical examples is presented in order to prove the performance of the method both in two- and three-dimensional scenarios. Finally, section 8 summarises a series of concluding remarks and points out some lines of further research.

2. Governing equations

2.1. Conservation law formulation

Consider the motion of a continuum from a reference domain (configuration) V to a spatial or deformed domain (configuration) v . The deformation is defined by a mapping $\boldsymbol{x} = \boldsymbol{x}(\boldsymbol{X}, t)$, where \boldsymbol{X} denotes the material position of a particle and \boldsymbol{x} its position in the deformed configuration (see Figure 1).

A mixed system of conservation laws was presented in [1] in order to describe the motion of the continuum as,

$$\frac{\partial \mathbf{p}}{\partial t} - \text{DIV } \mathbf{P} = \rho_0 \mathbf{b} \quad (1)$$

$$\frac{\partial \mathbf{F}}{\partial t} - \text{DIV } (\mathbf{v} \otimes \mathbf{I}) = \mathbf{0} \quad (2)$$

where $\mathbf{p} = \rho_0 \mathbf{v}$ is the linear momentum, ρ_0 is the initial material density, \mathbf{v} is the velocity field, \mathbf{b} is a body force per unit of mass, \mathbf{F} is the deformation gradient tensor and \mathbf{P} is the first Piola-Kirchhoff stress tensor. In addition, \mathbf{I} stands for the identity tensor and DIV describes the material divergence operator in undeformed configuration. The evolution equation (2) must be advanced in time satisfying a set of compatibility conditions (also known as involutions) for the deformation gradient \mathbf{F} [10, 50] which ensure that \mathbf{F} corresponds to the gradient of a real mapping, that is

$$\text{CURL}(\mathbf{F}) = \mathbf{0} \quad (3)$$

where CURL symbolises the material curl operator in undeformed configuration. Furthermore, since a Lagrangian description of the motion is used, the conservation of mass reduces to

$$\rho = \rho_0 J \quad (4)$$

where $J = \det(\mathbf{F})$ is the Jacobian of the deformation, which enables the explicit computation of the current density ρ at any stage of the deformation process. The system of equations (1)-(2) complemented with an adequate constitutive model can describe the motion of any isothermal hyperelastic material. However, for the case of thermo-mechanical materials, the energy equation (or first law of thermodynamics) must also be used to close the system, namely

$$\frac{\partial E_T}{\partial t} - \text{DIV } (\mathbf{P}^T \mathbf{v} - \mathbf{Q}) = r \quad (5)$$

where E_T is the total energy per unit of undeformed volume, \mathbf{Q} is the heat flux and r is a possible heat source. Finally, equations (1), (2) and (5) can be rewritten in a more compact form, describing a first order hyperbolic system as

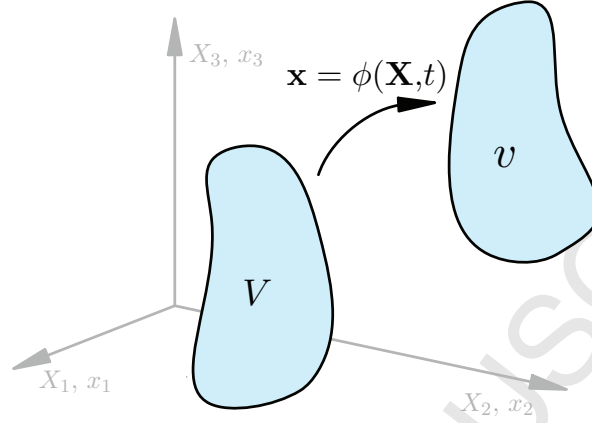


Figure 1: Deformation mapping

$$\frac{\partial \mathbf{u}}{\partial t} + \sum_I \frac{\partial \mathcal{F}_I}{\partial X_I} = \mathbf{s} \quad (6)$$

where in indicial notation

$$\mathbf{u} = \begin{pmatrix} p_1 \\ p_2 \\ p_3 \\ F_{11} \\ F_{12} \\ F_{13} \\ F_{21} \\ F_{22} \\ F_{23} \\ F_{31} \\ F_{32} \\ F_{33} \\ E_T \end{pmatrix}, \quad \mathcal{F}_I = \begin{pmatrix} -P_{1I}(\mathbf{F}) \\ -P_{2I}(\mathbf{F}) \\ -P_{3I}(\mathbf{F}) \\ -\delta_{I1}v_1 \\ -\delta_{I2}v_1 \\ -\delta_{I3}v_1 \\ -\delta_{I1}v_2 \\ -\delta_{I2}v_2 \\ -\delta_{I3}v_2 \\ -\delta_{I1}v_3 \\ -\delta_{I2}v_3 \\ -\delta_{I3}v_3 \\ Q_I - P_{iI}v_i \end{pmatrix}, \quad \mathbf{s} = \begin{pmatrix} \rho_0 b_1 \\ \rho_0 b_2 \\ \rho_0 b_3 \\ 0 \\ 0 \\ 0 \\ 0 \\ 0 \\ 0 \\ 0 \\ 0 \\ 0 \\ 0 \\ r \end{pmatrix}, \quad \forall I = 1, 2, 3 \quad (7)$$

2.2. Constitutive model: hyperelastic isothermal materials

The system of conservation laws (6) reduces, in the isothermal three dimensional case, to 12 equations and 21 unknowns. Therefore, additional relations are needed, in the form of a constitutive model, for the closure of the system. In the case of reversible isothermal elasticity, the first Piola-Kirchhoff tensor is defined as a function of the deformation gradient derived from an elastic energy potential $\psi(\mathbf{F})$ as (see for example [51–53])

$$\mathbf{P}(\mathbf{F}) = \frac{\partial \psi}{\partial \mathbf{F}}$$

where $\psi(\mathbf{F})$ has to satisfy objectivity and thermodynamic consistency (see for example [53]). Furthermore, the rank one convexity of the energy potential $\psi(\mathbf{F})$ ensures the hyperbolicity of the system (6) [51]. For nearly incompressible applications, it is often convenient to split this strain energy $\psi(\mathbf{F})$ into isochoric and volumetric components $\psi(\mathbf{F}) = \psi_{iso}(\hat{\mathbf{F}}) + \psi_{vol}(J)$, with $\hat{\mathbf{F}} = J^{-1/3}\mathbf{F}$, which in turn leads to the deviatoric and pressure components of \mathbf{P} as,

$$\mathbf{P} = \mathbf{P}_{dev} + \mathbf{P}_{vol}; \quad \mathbf{P}_{dev} = \frac{\partial \psi_{iso}}{\partial \mathbf{F}}, \quad \mathbf{P}_{vol} = \frac{\partial \psi_{vol}}{\partial \mathbf{F}}$$

In particular, the volumetric term can be further developed by introducing the pressure p as

$$\mathbf{P}_{vol} = pJ\mathbf{F}^{-T}; \quad p = \frac{d\psi_{vol}(J)}{dJ}$$

Note that the sign convention used here is p positive in tension and negative in compression. The simplest example of a constitutive model which satisfies the above form is given by the nearly incompressible extension of the neo-Hookean model defined by

$$\psi_{dev} = \mu [J^{-2/3}(\mathbf{F} : \mathbf{F}) - 3]; \quad \psi_{vol} = \frac{1}{2}\kappa(J - 1)^2$$

where μ and κ are the shear and bulk modulus, respectively. The resulting components of the first Piola-Kirchhoff stress tensor read

$$\mathbf{P} = \mu J^{-2/3} \left[\mathbf{F} - \frac{1}{3}(\mathbf{F} : \mathbf{F}) \mathbf{F}^{-T} \right] + pJ\mathbf{F}^{-T}, \quad p = \kappa(J - 1) \quad (8)$$

Combining this constitutive model with system (6) results in a hyperbolic system of equations with eigenvalues [1]

$$U_p = \pm \sqrt{\frac{\beta + \left(\frac{\alpha}{\Lambda^2} + 2\gamma\right)}{\rho_0}}; \quad U_s = \pm \sqrt{\frac{\beta}{\rho_0}} \quad (9)$$

which are the volumetric and shear wave speeds, U_p and U_s respectively, and

$$\alpha = \kappa J^2 + \frac{5}{9} \mu J^{-2/3} (\mathbf{F} : \mathbf{F}), \quad \beta = \mu J^{-2/3}, \quad \gamma = -\frac{2}{3} \mu J^{-2/3} \quad (10)$$

$$\Lambda = \frac{1}{\|\mathbf{F}^{-T} \mathbf{N}\|} \quad (11)$$

2.3. Constitutive model: hyperelastic-plastic material

In order to model plastic behaviour, a rate-independent von Mises plasticity model with isotropic hardening, such as that presented in [53, 54], is used. The deformation gradient tensor \mathbf{F} is multiplicatively decomposed into an elastic component \mathbf{F}_e and a plastic component \mathbf{F}_p as

$$\mathbf{F} = \mathbf{F}_e \mathbf{F}_p; \quad \mathbf{b}_e = \mathbf{F} \mathbf{C}_p^{-1} \mathbf{F}^T; \quad \mathbf{C}_p = \mathbf{F}_p^T \mathbf{F}_p \quad (12)$$

In addition, a strain energy functional in terms of the elastic principal stretches $(\lambda_{e,1}, \lambda_{e,2}, \lambda_{e,3})$ is defined as

$$\psi(\lambda_{e,1}, \lambda_{e,2}, \lambda_{e,3}) = \psi_{dev}(J^{-1/3} \lambda_{e,1}, J^{-1/3} \lambda_{e,2}, J^{-1/3} \lambda_{e,3}) + \psi_{vol}(J) \quad (13)$$

where

$$\psi_{dev} = \mu \left[(\ln \lambda_{e,1})^2 + (\ln \lambda_{e,2})^2 + (\ln \lambda_{e,3})^2 \right] - \frac{1}{3} \mu (\ln J)^2 \quad (14)$$

and

$$\psi_{vol} = \frac{1}{2} \kappa (\ln J)^2; \quad \ln J = \ln \lambda_{e,1} + \ln \lambda_{e,2} + \ln \lambda_{e,3} \quad (15)$$

The algorithm to update the plastic strain \mathbf{C}_p is summarised in Algorithm 2.1 [53].

Algorithm 2.1: EVALUATION OF $\mathbf{P}_{n+1}(\mathbf{F}_{n+1}, \mathbf{C}_{p,n}^{-1}, \bar{\varepsilon}_{p,n})$

- (1) Given \mathbf{F}_{n+1} , $\mathbf{C}_{p,n}^{-1}$ and $\bar{\varepsilon}_{p,n}$
- (2) Initiate $\Delta\gamma = \nu_\alpha^{n+1} = 0$
- (3) Evaluate $J_{n+1} = \det \mathbf{F}_{n+1}$
- (4) Solve pressure $p = \kappa \frac{\ln J_{n+1}}{J_{n+1}}$
- (5) Compute trial left strain tensor $\mathbf{b}_{e,n+1}^{trial} = \mathbf{F}_{n+1} \mathbf{C}_{p,n}^{-1} \mathbf{F}_{n+1}^T$
- (6) Spectral decomposition: $\mathbf{b}_{e,n+1}^{trial} = \sum_{\alpha=1}^3 (\lambda_{e,\alpha}^{trial})^2 \mathbf{n}_\alpha^{trial} \otimes \mathbf{n}_\alpha^{trial}$
- (7) Set $\mathbf{n}_\alpha^{n+1} = \mathbf{n}_\alpha^{trial}$
- (8) Trial Kirchhoff stress: $\tau'_{\alpha\alpha}{}^{trial} = 2\mu \ln \lambda_{e,\alpha}^{trial} - \frac{2}{3}\mu \ln J_{n+1}$
- if** ($f(\boldsymbol{\tau}'^{trial}, \bar{\varepsilon}_{p,n}) > 0$)
- then**
 - (9) Direction vector: $\nu_\alpha^{n+1} = \frac{\tau'_{\alpha\alpha}{}^{trial}}{\sqrt{\frac{2}{3}\|\boldsymbol{\tau}'^{trial}\|}}$
 - (10) Incremental plastic multiplier: $\Delta\gamma = \frac{f(\boldsymbol{\tau}'^{trial}, \bar{\varepsilon}_{p,n})}{3\mu+H}$
- (11) Elastic stretch: $\lambda_{e,\alpha}^{n+1} = \text{Exp}(\ln \lambda_{e,\alpha}^{trial} - \Delta\gamma \nu_\alpha^{n+1})$
- (12) Return map: $\tau'_{\alpha\alpha} = \left(1 - \frac{2\mu\Delta\gamma}{\sqrt{2/3}\|\boldsymbol{\tau}'^{trial}\|}\right) \tau'_{\alpha\alpha}{}^{trial}$
- (13) Update stress: $\tau_{\alpha\alpha} = \tau'_{\alpha\alpha} + Jp$; $\boldsymbol{\tau} = \sum_{\alpha=1}^3 \tau_{\alpha\alpha} \mathbf{n}_\alpha^{n+1} \otimes \mathbf{n}_\alpha^{n+1}$
- (14) First Piola-Kirchhoff stress tensor: $\mathbf{P} = \boldsymbol{\tau} \mathbf{F}^{-T}$
- (15) Update $\mathbf{b}_{e,n+1} = \sum_{\alpha=1}^3 (\lambda_{e,\alpha}^{n+1})^2 \mathbf{n}_\alpha^{n+1} \otimes \mathbf{n}_\alpha^{n+1}$
- (16) Update $\mathbf{C}_{p,n+1}^{-1} = \mathbf{F}_{n+1}^{-1} \mathbf{b}_{e,n+1} \mathbf{F}_{n+1}^{-T}$; $\bar{\varepsilon}_{p,n+1} = \bar{\varepsilon}_{p,n} + \Delta\gamma$
- return** (\mathbf{P}_{n+1})

2.4. Equation of state: Mie-Gruneisen

In order to take into account thermo-mechanical interaction, an equation of state needs to be provided for the closure of the system (1), (2), (5). In this paper, the Mie-Gruneisen equation of state is used, where the pressure p is defined in terms of the internal energy density e and the Jacobian J (see for example [55] or [11]),

$$p(e, J) = \frac{\kappa(J-1)}{(1-s(1-J))^2} - \frac{\Gamma(J)}{J} \left[e - \frac{1}{2}\kappa \left(\frac{(J-1)}{1-s(1-J)} \right)^2 \right] \quad (16)$$

where

$$\Gamma(J) = \Gamma_0 J^q \quad (17)$$

with Γ_0 , q and s material parameters obtained from experimental results and e the internal energy density which, in the absence of body forces, is defined as,

$$e = E_T - \frac{1}{2\rho_0} \mathbf{p} \cdot \mathbf{p} \quad (18)$$

3. JST Space discretisation

3.1. Dual mesh and area vectors

The JST scheme is a vertex centred Finite Volume Method and, as such, requires the use of a dual mesh for the definition of control volumes. In this paper, the median dual approach for triangular and tetrahedral meshes, as presented in [44] or [45], has been chosen. This approach constructs the dual mesh by connecting edge midpoints with element centroids in two dimensions (see Figure 2) and edge midpoints with face centroids and element centroids in three dimensions (see Figure 3). Such a configuration ensures no overlapping of the control volumes and, combined with central differences, is equivalent to standard Galerkin FEM discretisations when using linear elements (see References [34, 38–41]). For a given node a , the set of nodes connected to it through an edge is denoted by Λ_a and the subset of nodes connected to a through a boundary edge is written as Λ_a^B (see figure 2). For a given edge connecting nodes a and b , an area vector is then defined as

$$\mathbf{C}^{ab} = \sum_{k \in \Gamma_{ab}} A_k \mathbf{N}_k \quad (19)$$

where Γ_{ab} is the set of facets belonging to edge ab , A_k is the area of a given facet k and \mathbf{N}_k its normal. Due to the definition of the dual mesh, the area vectors satisfy $\mathbf{C}^{ab} = -\mathbf{C}^{ba}$. These area vectors enable a substantial reduction in the computational cost when computing the boundary integral used in the Green Gauss divergence theorem (classical in FVM), since they save an additional loop on facets. In the case of a boundary edge, the contribution of the boundary faces to which it belongs, has to be taken into account as well. This set of faces will be defined as Γ_a^B (see Figures 2b and 3b).

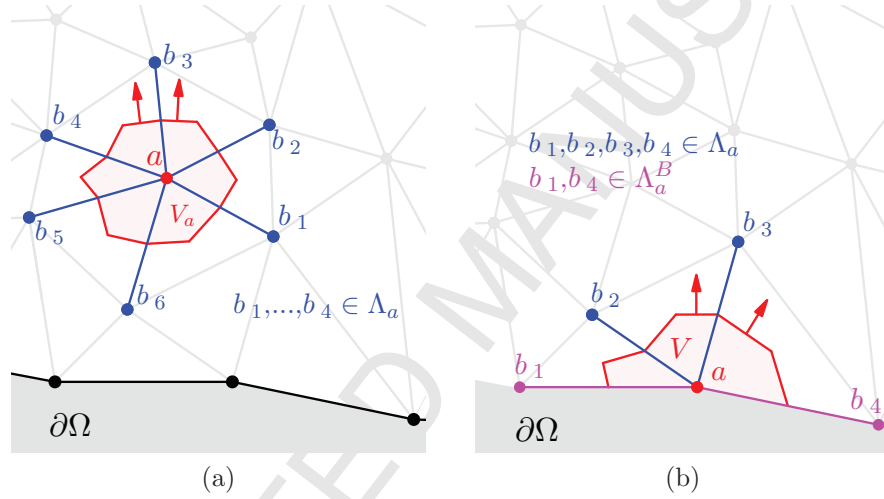


Figure 2: Control volume for an interior node (a) and boundary node (b) using the median dual approach in a triangular mesh. The red shaded area is the control volume associated to node a . The blue lines are the edges connecting node a to its neighbouring nodes b_i , that is, the set Λ_a . The magenta lines in (b) are the boundary edges connecting node a to its neighbouring nodes b_i , that is, the set Λ_a^B .

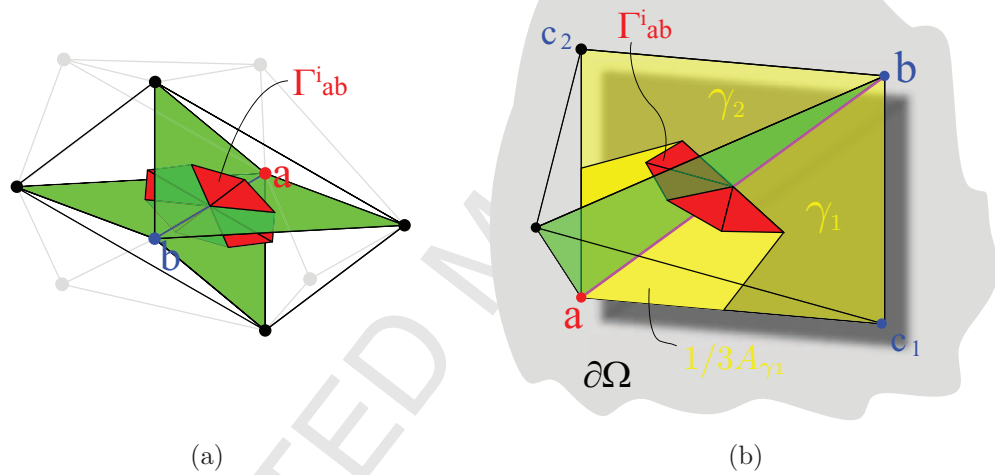


Figure 3: Set of facets related to an interior edge (a) and boundary edge (b) in three dimensions. The green surfaces correspond to the interior faces to which the edge belongs, whereas the dark yellow surfaces correspond to the boundary faces $\gamma_1 = \widehat{abc_1}$ and $\gamma_2 = \widehat{abc_2}$. The red surfaces are the set of interior facets Γ_{ab}^i corresponding to edge ab . The bright yellow zone is the tributary area of faces γ_1 and γ_2 to node a .

3.2. General JST scheme

Consider a hyperbolic system of conservation laws generally written as

$$\frac{\partial \mathbf{U}}{\partial t} + \sum_I \frac{\partial \mathcal{F}_I}{\partial X_I} = \mathbf{0} \quad (20)$$

where \mathbf{U} is the vector of conservation variables and \mathcal{F}_I the flux vector associated to the spatial direction I . By using a standard Finite Volume discretisation, the equations are integrated within a given control volume a followed by the divergence theorem to give,

$$\frac{d\mathbf{U}_a}{dt} = -\frac{1}{V_a} \int_{\partial V_a} \mathcal{F} \mathbf{N} dA \quad (21)$$

where \mathbf{U}_a is the average value of the variable within the control volume and \mathbf{N} is the normal vector of the control volume boundary. Equation (21) can be discretised in space by using central differences and JST type of stabilisation (see [44] and [45]) to give, for a given node a ,

$$\frac{d\mathbf{U}_a}{dt} = \frac{-1}{V_a} \left(\sum_{b \in \Lambda_a} \frac{\mathcal{F}_a + \mathcal{F}_b}{2} C^{ab} + \sum_{\gamma \in \Gamma_a^B} \mathcal{F}_a^\gamma \mathbf{N}^\gamma \frac{A^\gamma}{3} \right) + \frac{1}{V_a} \mathcal{D}(\mathbf{U}_a) \quad (22)$$

where \mathcal{F} is a matrix gathering the flux vectors in the three spatial directions as $\mathcal{F} = [\mathcal{F}_1, \mathcal{F}_2, \mathcal{F}_3]$ and $\mathcal{D}(\mathbf{U}_a)$ is a dissipative operator. The terms within the parenthesis in (22) correspond to the actual Green-Gauss evaluation of the control volume boundary fluxes, which is second order in space. This evaluation is composed of a summation over edges (first term in the parenthesis) and a summation over boundary faces (second term in the parenthesis). In this second term, the weighted average stencil proposed by [56] is employed, computing the flux over a face γ in three dimensions as

$$\mathcal{F}_a^\gamma = \frac{6\mathcal{F}_a + \mathcal{F}_b + \mathcal{F}_c}{8} \quad (23)$$

where b, c are the two nodes that together with node a define face γ . For the two dimensional case the above expression reads

$$\mathcal{F}_a^\gamma = \frac{5\mathcal{F}_a + \mathcal{F}_b}{6} \quad (24)$$

The dissipative operator is composed of a blend of second order differences (Laplacian operator) and fourth order differences (biharmonic operator). The fourth order differences avoid the appearance of the odd-even decoupling of the solution (that would result from using averaged fluxes) whilst maintaining the second order accuracy of the scheme. The second order differences are introduced to smear out the solution in the vicinity of a shock whilst reducing the solution to first order locally. This dissipative operator reads

$$\mathcal{D}(\mathbf{u}_a) = \sum_{b \in \Lambda_a} \varepsilon_{ab}^{(2)} \Psi_{ab} \theta_{ab} (\mathbf{u}_b - \mathbf{u}_a) - \varepsilon_{ab}^{(4)} \Psi_{ab} \theta_{ab} (\mathbf{L}(\mathbf{u}_b) - \mathbf{L}(\mathbf{u}_a)) \quad (25)$$

where $\varepsilon_{ab}^{(2)}$ and $\varepsilon_{ab}^{(4)}$ are discontinuity switches which activate either the second or fourth order differences, Ψ_{ab} is a coefficient (defined below) computed on the basis of the spectral radius of the flux Jacobian matrix and θ_{ab} denote geometrical weights which approximate the non divided Laplacian, \mathbf{L} , as,

$$\mathbf{L}(\mathbf{u}_a) = \sum_{b \in \Lambda_a} \theta_{ab} (\mathbf{u}_b - \mathbf{u}_a) \quad (26)$$

The geometrical weights θ_{ab} are used to preserve the second order accuracy, given by the central differences, when adding the numerical dissipation. In the current paper, the geometrical weights as proposed by [37] are used, these are defined as

$$\theta_{ab} = 1 - \boldsymbol{\lambda}_{ab} \cdot (\mathbf{X}^b - \mathbf{X}^a) \quad (27)$$

where $\boldsymbol{\lambda}_{ab}$ is the solution to the following system of equations

$$\mathbf{K}^{ab} \boldsymbol{\lambda}_{ab} = \mathbf{b}^{ab}$$

where

$$\begin{aligned} \mathbf{K}^{ab} &= \sum_{b \in \Lambda_a} (\mathbf{X}^b - \mathbf{X}^a) \otimes (\mathbf{X}^b - \mathbf{X}^a) \\ \mathbf{b}^{ab} &= \sum_{b \in \Lambda_a} (\mathbf{X}^b - \mathbf{X}^a) \end{aligned}$$

It is clear from (27) that $\theta_{ab} \neq \theta_{ba}$ and, therefore, this will affect the conservation of the variables when adding the artificial dissipation. This issue will

be addressed later in the paper, by using a modified dissipation term such that satisfaction of the conservation of the primary variables is ensured. The pressure switches $\varepsilon_{ab}^{(2)}$ and $\varepsilon_{ab}^{(4)}$ are written as

$$\varepsilon_{ab}^{(2)} = \kappa^{(2)} \max(\Upsilon_a, \Upsilon_b) \quad (28)$$

$$\varepsilon_{ab}^{(4)} = \max \left[0, (\kappa^{(4)} - \varepsilon_{ab}^{(2)}) \right] \quad (29)$$

where $\kappa^{(2)}$ and $\kappa^{(4)}$ are the dissipation factors and Υ is a normalized second order difference of some conserved variable. For the discretisation of the Euler equations as in [33, 34], these differences are computed using the fluid pressure, p , as

$$\Upsilon_a = \frac{|\sum_{b \in \Lambda_a} \theta_{ab}(p_b - p_a)|}{\sum_{b \in \Lambda_a} (p_b + p_a)} \quad (30)$$

Finally, the artificial dissipation requires a scaling, which is obtained by using the spectral radius. The spectral radius is defined as

$$\Psi_{ab} = \frac{1}{2} [\Psi_a + \Psi_b], \quad \Psi_a = \sum_{k \in \partial\Omega_a} |\lambda| A_k \quad (31)$$

where $|\lambda|$ is the maximum eigenvalue of the flux Jacobian matrix of the system of conservation equations (20). In the particular case of the Euler equations, this corresponds to $|\lambda| = |c + u|$ where c and u are, respectively, the speed of the sound and the velocity of the fluid. In our case, this is simply U_p , the speed of the pressure wave.

It is worthwhile mentioning that the JST scheme is a well known artificial dissipation scheme, with properties that have been extensively studied by previous authors in the CFD community [33, 57, 58]. Specifically, reference [59], proves that the JST scheme is Local Extremum Diminishing (LED) provided that the artificial dissipation is scaled with the average of the maximum eigenvalue of the flux Jacobian matrix (see spectral radius in equation (31)) and that a pressure switch is used (see equation (25)) in the presence of shocks. Satisfaction of the LED condition ensures that numerical dissipation is added into the solution with the subsequent increase in entropy.

3.3. Discretisation of the governing equations

For the discretisation of the governing equations (1,2,5), it transpires that dissipation only needs to be added to the first equation. The discretised equations read

$$\frac{d\mathbf{p}_a}{dt} = \frac{1}{V_a} \left(\sum_{\alpha \in \Lambda_a} \frac{1}{2} (\mathbf{P}_\alpha + \mathbf{P}_b) \mathbf{C}^{ab} + \sum_{\gamma \in \Gamma_a^B} \hat{\mathbf{t}}_a^\gamma \frac{A^\gamma}{3} \right) + \frac{1}{V_a} \mathcal{D}(\mathbf{p}_a) \quad (32)$$

$$\frac{d\mathbf{F}_a}{dt} = \frac{1}{V_a} \left(\sum_{\alpha \in \Lambda_a} \frac{\mathbf{v}_\alpha + \mathbf{v}_b}{2} \otimes \mathbf{C}^{ab} + \sum_{\gamma \in \Gamma_a^B} (\hat{\mathbf{v}}_a^\gamma \otimes \mathbf{N}^\gamma) \frac{A^\gamma}{3} \right) \quad (33)$$

$$\frac{dE_{T_a}}{dt} = \frac{1}{V_a} \left(\sum_{\alpha \in \Lambda_a} \frac{1}{2} (\mathbf{P}_\alpha^T \mathbf{v}_\alpha + \mathbf{P}_b^T \mathbf{v}_b) \cdot \mathbf{C}^{ab} + \sum_{\gamma \in \Gamma_a^B} (\hat{\mathbf{v}}_a^\gamma \cdot \hat{\mathbf{t}}_a^\gamma) \frac{A^\gamma}{3} \right) \quad (34)$$

where $\hat{\mathbf{t}}_a^\gamma$ and $\hat{\mathbf{v}}_a^\gamma$ are the corrected face tractions and velocities that will lead to the imposition of the weak boundary conditions.

The time evolution of the deformation gradient \mathbf{F} in equation (33) is carried out without the introduction of numerical dissipation. This discrete space-time evolution equation yields a discrete update of \mathbf{F} which is curl-free at a discrete level, as the right hand side of equation (33) represents a central difference stencil. With this update and provided that the initial conditions are curl free, it is then possible to guarantee the existence of a discrete deformation gradient tensor which satisfies the necessary involutions [1, 10, 60].

Due to the absence of physical shocks in the examples presented in this paper, the dissipation operator will be reduced to the fourth order dissipation term (see equation (25))

$$\mathcal{D}(\mathbf{p}_a) = - \sum_{b \in \Lambda_a} \kappa^{(4)} \Psi_{ab} \theta_{ab} (\mathbf{L}(\mathbf{p}_b) - \mathbf{L}(\mathbf{p}_a)) \quad (35)$$

3.4. Boundary conditions

The boundary conditions will be imposed weakly using the discretised equations (32) and (33). Four different types of boundary conditions will be considered: free boundary, tangentially sliding boundary, normally sliding

boundary and clamped boundary (see Figure 4). Given a boundary face γ , the non-corrected velocity and traction at the boundary are defined as

$$\mathbf{t}_a^\gamma = \frac{6\mathbf{P}_a + \mathbf{P}_b + \mathbf{P}_c}{8} \mathbf{N}^\gamma \quad (36)$$

$$\mathbf{v}_a^\gamma = \frac{6\mathbf{v}_a + \mathbf{v}_b + \mathbf{v}_c}{8} \quad (37)$$

The velocities and tractions are corrected as follows,

Clamped boundary

$$\hat{\mathbf{t}}_a^\gamma = \mathbf{t}_a^\gamma \quad (38a)$$

$$\hat{\mathbf{v}}_a^\gamma = \mathbf{0} \quad (38b)$$

Free boundary

$$\hat{\mathbf{t}}_a^\gamma = \mathbf{t}^B \quad (39a)$$

$$\hat{\mathbf{v}}_a^\gamma = \mathbf{v}_a^\gamma \quad (39b)$$

Normally sliding boundary

$$\hat{\mathbf{t}}_a^\gamma = (\mathbf{I} - \mathbf{N} \otimes \mathbf{N})\mathbf{t}_a^\gamma + (\mathbf{N} \otimes \mathbf{N})\mathbf{t}^B \quad (40a)$$

$$\hat{\mathbf{v}}_a^\gamma = (\mathbf{N} \otimes \mathbf{N})\mathbf{v}_a^\gamma \quad (40b)$$

Tangentially sliding boundary

$$\hat{\mathbf{t}}_a^\gamma = (\mathbf{N} \otimes \mathbf{N})\mathbf{t}_a^\gamma + (\mathbf{I} - \mathbf{N} \otimes \mathbf{N})\mathbf{t}^B \quad (41a)$$

$$\hat{\mathbf{v}}_a^\gamma = (\mathbf{I} - \mathbf{N} \otimes \mathbf{N})\mathbf{v}_a^\gamma \quad (41b)$$

4. Time integration

The time discretisation is performed using a Total Variation Diminishing (TVD) Runge-Kutta time integrator as proposed by Shu and Osher [49, 61]. For a set of equations discretised in space, but left continuous in time (method

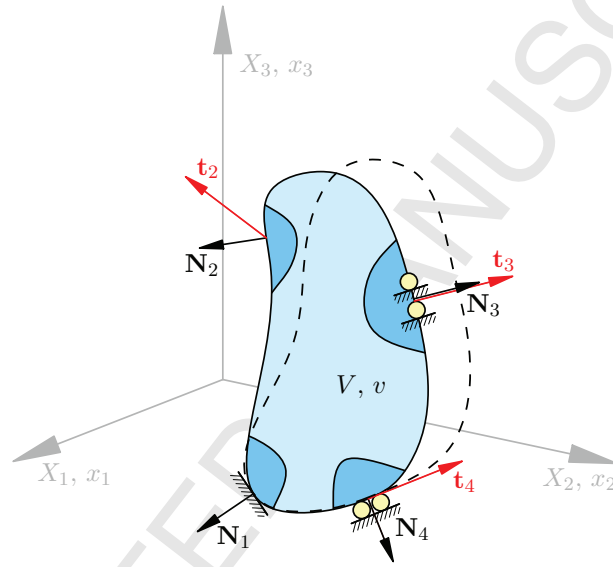


Figure 4: The boundary conditions are imposed at the reference configuration. The continuous line represents the body at the reference (undeformed) configuration, while the discontinuous line the body at the spatial (deformed) configuration. Four different types of boundary conditions are considered: clamped boundary (condition 1), free boundary (condition 2), normally sliding boundary (condition 3) and tangentially sliding boundary (condition 4).

of lines) at a given node a , the following system of ordinary differential equations (ODEs) is defined

$$\frac{d\mathbf{u}_a}{dt} = -\mathcal{R}_a(\mathbf{u}_a, t) \quad (42)$$

The Runge-Kutta method computes the solution at time step t^{n+1} from the solution at time step t^n as

$$\begin{aligned} \mathbf{u}_a^* &= \mathbf{u}_a^n - \Delta t \mathcal{R}_a(\mathbf{u}_a^n, t^n) \\ \mathbf{u}_a^{**} &= \mathbf{u}_a^* - \Delta t \mathcal{R}_a(\mathbf{u}_a^*, t^{n+1}) \\ \mathbf{u}_a^{n+1} &= \frac{1}{2} (\mathbf{u}_a^n + \mathbf{u}_a^{**}) \end{aligned} \quad (43)$$

where the time step is governed by a standard Courant—Friedrichs—Lewy (CFL) condition (see for example [28, 41, 45]),

$$\Delta t \leq \alpha_{CFL} \min_a \left(\frac{h_a}{(U_p)_a^n} \right) \quad (44)$$

where h_a is the minimum length across the control volume of node a at the reference domain, $(U_p)_a^n$ is the volumetric wave speed as presented in equation (9) and α_{CFL} is the CFL stability number.

In addition, the displacements are integrated in time using the trapezoidal rule as,

$$\mathbf{x}_a^{n+1} = \mathbf{x}_a^n + \frac{\Delta t}{2} (\mathbf{v}_a^n + \mathbf{v}_a^{n+1}) \quad (45)$$

5. Discrete angular and linear momentum conserving algorithm

Since the conservation variables are linear momentum, deformation gradient and total energy, the proposed scheme does not necessarily preserve the angular momentum of the system. Furthermore, as stated in section 3, the artificial dissipation term prevents the exact conservation of linear momentum due to the lack of symmetry of the geometrical weights. The current section presents an adaptation of the angular momentum conservation algorithm presented in [1] that will modify the internal tractions and dissipation in order to preserve both linear and angular momentum.

In the absence of external tractions, the conservation of the discrete angular momentum after a time step can be written as

$$\sum_{a=1}^{N_{nodes}} \mathbf{x}_a^{n+1} \times m_a \mathbf{v}_a^{n+1} - \sum_{a=1}^{N_{nodes}} \mathbf{x}_a^n \times m_a \mathbf{v}_a^n = \mathbf{0} \quad (46)$$

By taking into account the trapezoidal rule for the time integration of the positions (see equation (45)), the above equation can be rewritten as

$$\sum_{a=1}^{N_{nodes}} \mathbf{x}_a^{n+1/2} \times m_a \Delta \mathbf{v}_a = \mathbf{0}; \quad \Delta \mathbf{v}_a = \mathbf{v}_a^{n+1} - \mathbf{v}_a^n; \quad \mathbf{x}_a^{n+1/2} = \mathbf{x}_a^n + \frac{\Delta t}{2} \mathbf{v}_a^n \quad (47)$$

Considering the TVD Runge-Kutta time integration as presented in the previous section, the velocity reads

$$\Delta \mathbf{v}_a = -\frac{\Delta t}{2\rho_0} (\mathcal{R}_a^n(\mathbf{p}_a^n, t^n) + \mathcal{R}_a^*(\mathbf{p}_a^*, t^*)) \quad (48)$$

where $\mathcal{R}_a(\mathbf{p}_a, t)$ corresponds to the right hand side of equation (32). Substituting equation (48) into (47), the following equation is obtained

$$\sum_{e=1}^{N_{nodes}} \mathbf{x}_a^{n+1/2} \times m_a \left(-\frac{\Delta t}{2\rho_0} (\mathcal{R}_a^n(\mathbf{p}_a^n, t^n) + \mathcal{R}_a^*(\mathbf{p}_a^*, t^*)) \right) = \mathbf{0}. \quad (49)$$

A sufficient condition to satisfy the above equation is given when the following equation

$$\sum_{a=1}^{N_{nodes}} \mathbf{x}_a^{n+1/2} \times m_a \mathcal{R}_a^\alpha(\mathbf{p}_a^\alpha, t^\alpha) = \mathbf{0} \quad (50)$$

is satisfied at the two time stages of the Runge-Kutta time integrator (i.e., $\forall \alpha \in \{n, *\}$). Replacing the right hand side of equation (32) into (50) and omitting the time superindex for simplicity, the following equation is obtained

$$\sum_{a=1}^{N_{nodes}} \mathbf{x}_a \times \frac{m_a}{\rho_0 V_a} \left(\sum_{\alpha \in \Lambda_a} \frac{1}{2} (\mathbf{P}_a + \mathbf{P}_b) \mathbf{C}^{ab} + \sum_{\gamma \in \Gamma_a^B} \hat{\mathbf{t}}_a^\gamma \frac{A^\gamma}{3} + \mathcal{D}(\mathbf{p}_a) \right) = \mathbf{0} \quad (51)$$

Assuming a free boundary traction (that could otherwise contribute to an external torque) and rearranging the first term into a summation over edges, the equation above is simplified to

$$\sum_{k=1}^{N_{ed_{int}}} \mathbf{f}_k \times (\mathbf{x}_b - \mathbf{x}_a) + \sum_{a=1}^{N_{nodes}} \mathcal{D}(\mathbf{p}_a) \times \mathbf{x}_a = \mathbf{0} \quad (52)$$

where the fact that $\mathbf{C}^{ab} = -\mathbf{C}^{ba}$ has been considered and where $\mathbf{f}_k = \frac{1}{2}(\mathbf{P}_a + \mathbf{P}_b)\mathbf{C}^{ab}$ is the force related to edge k . A sufficient condition for fulfilling the above equation is satisfied when both terms separately vanish. For the internal forces, this reads

$$\sum_{k=1}^{N_{ed_{int}}} \mathbf{f}_k \times \Delta \mathbf{x} = \mathbf{0} \quad (53)$$

where $\Delta \mathbf{x} = \mathbf{x}_b^{n+1/2} - \mathbf{x}_a^{n+1/2}$. As explained in section 3 the geometrical weights are not symmetric and, therefore, the conservation of linear momentum would not be satisfied. An extra condition has to be added for the satisfaction of such condition which, together with the angular momentum preservation condition, reads

$$\sum_{a=1}^{N_{nodes}} \mathcal{D}(\mathbf{p}_a) \times \mathbf{x}_a = \mathbf{0} \quad (54a)$$

$$\sum_{e=1}^{N_{nodes}} \mathcal{D}(\mathbf{p}_e) = \mathbf{0} \quad (54b)$$

A Lagrangian minimisation procedure has to be used to obtain a modified set of internal forces, $\hat{\mathbf{f}}_k$ that satisfy equation (53) and a set of modified dissipation $\hat{\mathcal{D}}(\mathbf{p}_e)$ that satisfy both equations (54a) and (54b). This is achieved by minimising the following two functionals

$$\Pi_f(\hat{\mathbf{f}}_k, \lambda_f) = \left(\frac{1}{2} \sum_{k=1}^{N_{ed_{int}}} (\hat{\mathbf{f}}_k - \mathbf{f}_k) \cdot (\hat{\mathbf{f}}_k - \mathbf{f}_k) \right) + \lambda_f \cdot \sum_{k=1}^{N_{ed_{int}}} \hat{\mathbf{f}}_k \times \Delta \mathbf{x}_k \quad (55)$$

$$\begin{aligned} \Pi_D(\hat{\mathcal{D}}(\mathbf{p}_a), \boldsymbol{\lambda}_D, \boldsymbol{\mu}_D) &= \left(\frac{1}{2} \sum_{a=1}^{N_{nodes}} (\hat{\mathcal{D}}(\mathbf{p}_a) - \mathcal{D}(\mathbf{p}_a)) \cdot (\hat{\mathcal{D}}(\mathbf{p}_a) - \mathcal{D}(\mathbf{p}_a)) \right) \\ &+ \boldsymbol{\lambda}_D \cdot \sum_{a=1}^{N_{nodes}} \hat{\mathcal{D}}(\mathbf{p}_a) \times \mathbf{x}_a + \boldsymbol{\mu}_D \cdot \sum_{a=1}^{N_{nodes}} \hat{\mathcal{D}}(\mathbf{p}_a) \end{aligned} \quad (56)$$

After some algebra a modified set of internal forces $\hat{\mathbf{f}}_k$ is obtained as

$$\hat{\mathbf{f}}_k = \mathbf{f}_k + \boldsymbol{\lambda}_f \times \Delta \mathbf{x}_k$$

where $\boldsymbol{\lambda}_f$ is the solution to the following system of 3×3 equations

$$\mathbf{K}_f \boldsymbol{\lambda}_f = \mathbf{b}_f$$

and where

$$\mathbf{K}_f = \sum_{k=1}^{N_{ed_{int}}} (\Delta \mathbf{x}_k \cdot \Delta \mathbf{x}_k) \mathbf{I} - \Delta \mathbf{x}_k \otimes \Delta \mathbf{x}_k \quad (57a)$$

$$\mathbf{b}_f = \sum_{k=1}^{N_{ed_{int}}} \mathbf{f}_k \times \Delta \mathbf{x}_k \quad (57b)$$

In a similar fashion, the minimisation of the functional described on equation (56) gives a modified set of dissipation at nodes

$$\hat{\mathcal{D}}(\mathbf{p}_a) = \mathcal{D}(\mathbf{p}_a) + \boldsymbol{\lambda}_D \times \mathbf{x}_a - \boldsymbol{\mu}_D \quad (58)$$

where $\boldsymbol{\lambda}_D$ is the solution to

$$\mathbf{K}_D \boldsymbol{\lambda}_D = \mathbf{b}_D$$

where

$$\mathbf{K}_D = \sum_{a=1}^{N_{nodes}} ((\mathbf{x}_a \cdot \mathbf{x}_a) \mathbf{I} - \mathbf{x}_a \otimes \mathbf{x}_a) - \frac{1}{N_{nodes}} ((\mathbf{a} \cdot \mathbf{a}) \mathbf{I} - \mathbf{a} \otimes \mathbf{a}) \quad (59a)$$

$$\mathbf{b}_D = \sum_{a=1}^{N_{nodes}} \mathcal{D}(\mathbf{p}_a) \times \mathbf{x}_a - \frac{1}{N_{nodes}} \mathbf{c} \times \mathbf{a} \quad (59b)$$

and the notation $\mathbf{a} = \sum_{a=1}^{N_{nodes}} \mathbf{x}_a$ and $\mathbf{c} = \sum_{a=1}^{N_{nodes}} \mathbf{D}(\mathbf{p}_a)$ has been used. Finally $\boldsymbol{\mu}_D$ is obtained as

$$\boldsymbol{\mu}_D = \frac{1}{N_{nodes}} \left(\sum_{a=1}^{N_{nodes}} \mathbf{D}(\mathbf{p}_a) + \boldsymbol{\lambda}_D \times \mathbf{a} \right) \quad (60)$$

This correction results into the computation of three global parameters $\boldsymbol{\lambda}_f$, $\boldsymbol{\lambda}_D$ and $\boldsymbol{\mu}_D$, which can be computed very efficiently within the spatial discretisation routines, as it will be explained in the next section.

6. Solution procedure

The algorithm 6.1 presents the solution procedure used for the update of the primary variables after a time step. The algorithm requires a preprocessing step for the computation of the geometrical variables $(\theta_{ab}, \mathbf{C}_{ab})$ related to the dual mesh. Once this is obtained, the algorithm only requires two

loops over edges and one loop over boundary faces per time stage.

Algorithm 6.1: EVALUATION OF $\mathcal{U}_{n+1}(\mathcal{U}_n)$

- (1) GIVEN $\mathcal{U}_a^n = (\mathbf{p}_a^n, \mathbf{F}_a^n)^T, \mathbf{x}_a^n$
- (2) LOOP over Runge-Kutta stages (to compute $\mathcal{U}_a^*, \mathcal{U}_a^{**}$)
 - (2.1) LOOP over edges $k(ab)$

$$\mathbf{L}(\mathbf{p}_a^n) := \mathbf{L}(\mathbf{p}_a^n) + \theta_{ab}(\mathbf{p}_b^n - \mathbf{p}_a^n)$$

$$\mathbf{L}(\mathbf{p}_b^n) := \mathbf{L}(\mathbf{p}_b^n) + \theta_{ba}(\mathbf{p}_a^n - \mathbf{p}_b^n)$$

$$\mathbf{b}_f := \mathbf{b}_f + \mathbf{f}_k \times \Delta \mathbf{x}_k^{n+1/2}$$

$$\mathbf{K}_f := \mathbf{K}_f + (\Delta \mathbf{x}_k^{n+1/2} \cdot \Delta \mathbf{x}_k^{n+1/2}) \mathbf{I} - \Delta \mathbf{x}_k^{n+1/2} \otimes \Delta \mathbf{x}_k^{n+1/2}$$
 - (2.2) COMPUTE $\lambda_f = \mathbf{K}_f^{-1} \mathbf{b}_f$
 - (2.3) LOOP over edges $k(ab)$

$$\hat{\mathbf{f}}_k^n = \mathbf{f}_k^n + \lambda_f \times \Delta \mathbf{x}_k^{n+1/2}$$

$$\hat{\mathcal{R}}_{p,a}^n := \hat{\mathcal{R}}_{p,a}^n + \hat{\mathbf{f}}_k$$

$$\mathcal{R}_{F,a}^n := \mathcal{R}_{F,a}^n + \frac{1}{2}(\mathbf{v}_a + \mathbf{v}_b) \otimes \mathbf{C}^{ab}$$

$$\mathcal{D}(\mathbf{p}_a) := \mathcal{D}(\mathbf{p}_a) - \kappa^{(4)} \Psi_{ab} \theta_{ab} (\mathbf{L}(\mathbf{p}_b) - \mathbf{L}(\mathbf{p}_a))$$

(proceed equivalently for node b)
 - (2.4) LOOP over boundary faces $\gamma(abc)$

$$\hat{\mathbf{t}}_a^\gamma, \hat{\mathbf{t}}_b^\gamma, \hat{\mathbf{t}}_c^\gamma, \hat{\mathbf{v}}_a^\gamma, \hat{\mathbf{v}}_b^\gamma, \hat{\mathbf{v}}_c^\gamma \text{ according to B.C.}$$

$$\hat{\mathcal{R}}_{p,a}^n := \hat{\mathcal{R}}_{p,a}^n + \hat{\mathbf{t}}_a^\gamma \frac{A^\gamma}{3}$$

$$\mathcal{R}_{F,a}^n := \mathcal{R}_{F,a}^n + (\hat{\mathbf{v}}_a^\gamma \otimes \mathbf{N}^\gamma) \frac{A^\gamma}{3}$$

(proceed equivalently for nodes b, c)
 - (2.5) COMPUTE λ_D, μ_D and modified dissipation

$$\hat{\mathcal{D}}(\mathbf{p}_a) = \mathcal{D}(\mathbf{p}_a) + \lambda_D \times \mathbf{x}_a^{n+1} - \mu_D$$
 - (2.6) UPDATE conservation variables at stage

$$\mathbf{p}_a^* = \mathbf{p}_a^n + \frac{1}{V_a} \left(\hat{\mathcal{R}}_{p,a}^n + \hat{\mathcal{D}}(\mathbf{p}_a) \right)$$

$$\mathbf{F}_a^* = \mathbf{F}_a^n + \frac{1}{V_a} \mathcal{R}_{F,a}^n$$
 - (2.7) EVALUATE $\mathbf{P}_a^* = \mathbf{P}(\mathbf{F}_a^*)$ (only after stage 1)
 - (2.8) APPLY strong BC
- (3) UPDATE conservation variables and positions

$$\mathcal{U}_a^{n+1} = \frac{1}{2} (\mathcal{U}_a^n + \mathcal{U}_a^{**})$$

$$\mathbf{x}_a^{n+1} = \mathbf{x}_a^n + \frac{\Delta t}{2} (\mathbf{v}_a^n + \mathbf{v}_a^{n+1})$$
- (4) EVALUATE $\mathbf{P}_a^{n+1} = \mathbf{P}(\mathbf{F}_a^{n+1})$
- (5) APPLY strong BC

7. Numerical examples

A series of numerical examples are included in this section in order to demonstrate the robustness, convergence and conservation properties of the formulation.

7.1. Low dispersion cube

This first example is a test case with an available closed form solution chosen in order to assess the numerical accuracy of the algorithm in the linear elastic regime. A cube of 1 m side has symmetric boundary conditions (constrained normal displacement) at the faces $X_1 = 0$ m, $X_2 = 0$ m and $X_3 = 0$ m and skew-symmetric boundary conditions (constrained tangential displacement) at the opposite faces, $X_1 = 1$ m, $X_2 = 1$ m and $X_3 = 1$ m. For the small strain case, the problem has an analytical solution of the type

$$\mathbf{u} = U_0 \cos\left(\frac{\sqrt{3}}{2}c_d\pi t\right) \begin{bmatrix} A \sin\left(\frac{\pi X_1}{2}\right) \cos\left(\frac{\pi X_2}{2}\right) \cos\left(\frac{\pi X_3}{2}\right) \\ B \cos\left(\frac{\pi X_1}{2}\right) \sin\left(\frac{\pi X_2}{2}\right) \cos\left(\frac{\pi X_3}{2}\right) \\ C \cos\left(\frac{\pi X_1}{2}\right) \cos\left(\frac{\pi X_2}{2}\right) \sin\left(\frac{\pi X_3}{2}\right) \end{bmatrix}$$

where A , B and C are constants such that $A + B + C = 0$ ¹ and $c_d = \sqrt{\frac{\mu}{\rho_0}}$. The problem is considered linear when $U_0 < 1 \times 10^{-3}$ m and, after applying a linear elastic constitutive model and imposing compatible initial conditions, the solution both for stresses and displacements can be computed at any time t . For the current example, a linear elastic material is chosen with a Poisson's ratio of $\nu = (1 - \mu/\kappa)/2 = 0.45$, Young's modulus $E = 1.7 \times 10^7$ Pa and density $\rho_0 = 1.1 \times 10^3$ kg/m³. The solution parameters are set as $A = 1$, $B = 1$ and $C = -2$ and $U_0 = 5 \times 10^{-4}$ m. Figure 5 shows the deformed shape of the cube as it evolves in time, and the values of the off-diagonal components of the first Piola-Kirchhoff stress tensor \mathbf{P} . The convergence error is analysed at time $t = 4 \times 10^{-3}$ s both for the stress and linear momentum components and for the L^1 and L^2 norms. Results are shown in Figure 6 and Figure 7. Crucially, it can be seen how the solution tends to asymptotic quadratic convergence for both stresses and velocities as the mesh is refined.

¹When $A + B + C = 0$ the volumetric deformation is zero since $\nabla^2 \mathbf{u} = 0$

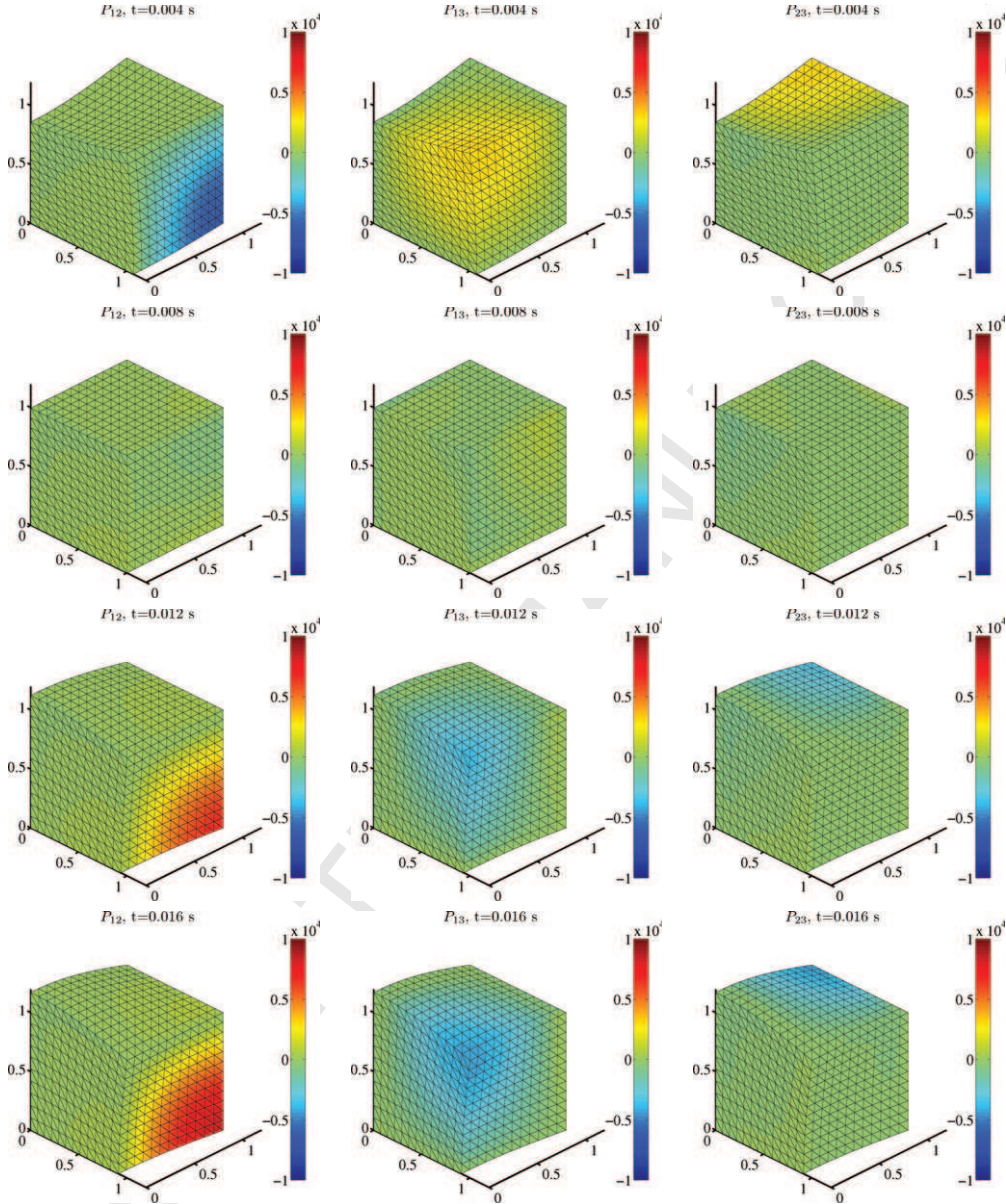


Figure 5: Linear elasticity three dimensional case. Snapshots at different times of the off diagonal components of the first Piola Kirchhoff stress tensor. Solution using $A = 1$, $B = 1$ and $C = -2$ and $U_0 = 5 \times 10^{-4}$ m. Linear elastic material with Poisson's ratio $\nu = 0.45$, Young's modulus $E = 1.7 \times 10^7$ Pa and density $\rho_0 = 1.1 \times 10^3$ kg/m³. JST spatial discretisation with $h = 1/12$ m, $\kappa^{(4)} = 1/128$ and $\alpha_{CFL} = 0.4$. Displacements scaled 100 times.

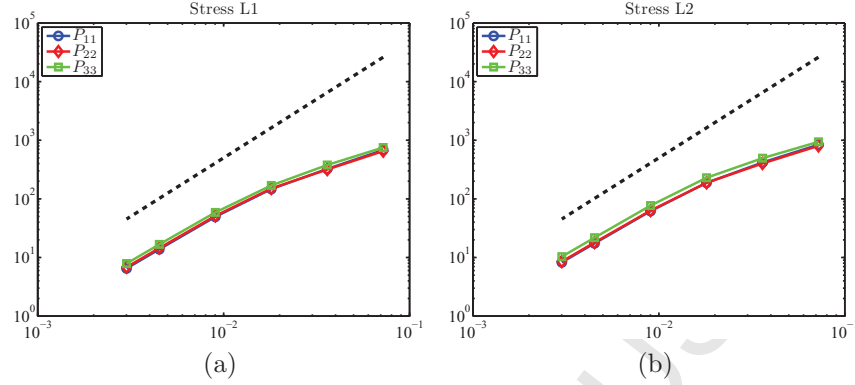


Figure 6: Linear elasticity three dimensional case. Convergence error for the stress components P_{11} , P_{22} and P_{33} in L^1 and L^2 norms at time $t = 0.004$ s as compared to the analytical solution. Solution using $A = 1$, $B = 1$ and $C = -2$ and $U_0 = 5 \times 10^{-4}$ m. Linear elastic material with Poisson's ratio $\nu = 0.45$, Young's modulus $E = 1.7 \times 10^7$ Pa and density $\rho_0 = 1.1 \times 10^3$ kg/m³. JST spatial discretisation with $h = 1/12$ m, $\kappa^{(4)} = 1/128$ and $\alpha_{CFL} = 0.4$.

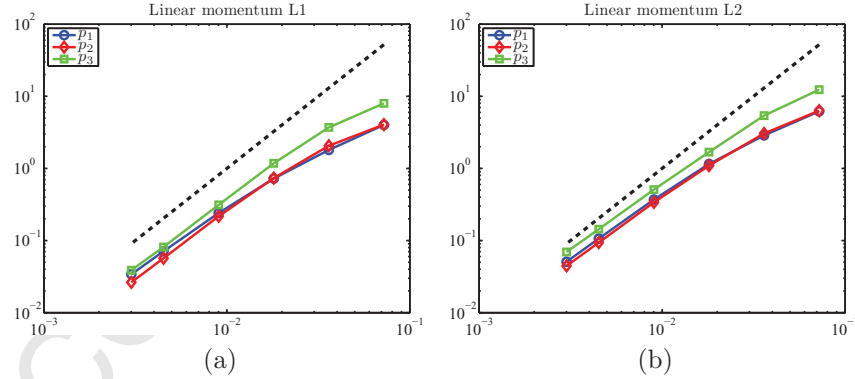


Figure 7: Linear elasticity three dimensional case. Convergence error for the linear momentum components in L^1 and L^2 norms at time $t = 0.004$ s as compared to the analytical solution. Solution using $A = 1$, $B = 1$ and $C = -2$ and $U_0 = 5 \times 10^{-4}$ m. Linear elastic material with Poisson's ratio $\nu = 0.45$, Young's modulus $E = 1.7 \times 10^7$ Pa and density $\rho_0 = 1.1 \times 10^3$ kg/m³. JST spatial discretisation with $h = 1/12$ m, $\kappa^{(4)} = 1/128$ and $\alpha_{CFL} = 0.4$.

7.2. Elastic vibration of a Beryllium plate

This example, designed to evaluate the accuracy of the method in the elastic regime, was previously published in [9, 62]. A Beryllium plate with no supports or constraints, of 6 cm length and 1 cm width, and material properties $\rho_0 = 1845 \text{ Kg/m}^3$, $E = 3.1827 \times 10^{11} \text{ Pa}$ and $\nu = 0.05390$ has an initial velocity of the form (see Figure 8),

$$\begin{aligned} \mathbf{v}_0 &= (0, v(X_1))^T \text{ m/s} \\ v(X_1) &= A\omega[g_1 (\sinh(\Omega(X_1 + 0.03)) + \sin(\Omega(X_1 + 0.03))) - \\ &\quad g_2 (\cosh(\Omega(X_1 + 0.03)) + \cos(\Omega(X_1 + 0.03)))] \end{aligned}$$

where [9, 62]

$$\begin{aligned} g_1 &= 56.637, \quad g_2 = 57.646, \quad \omega = 2.3597 \times 10^5 \text{ s}^{-1}, \quad A = 4.3369 \times 10^{-5} \text{ m} \\ \Omega &= 78.834 \text{ m}^{-1} \end{aligned}$$

which excites its first flexural mode [62]. In order to reproduce the same results as in [9], the material model is chosen as a hyperelastic-plastic (Von Mises) with yield strength $Y^0 = 1 \times 10^{11} \text{ Pa}$, which is high enough to avoid any plastic deformation of the plate. Figure 9 shows the evolution in time of the norm of the velocity vector. Results compare very well with those provided in [9].

In Figure 10, the evolution in time of the internal and kinetic energies are compared against the total energy (solution of equation (5) for three different mesh refinements). In the absence of plasticity and heat effects, the difference between the total energy (black discontinuous line) and the summation of the internal and kinetic energies (green line) is the actual dissipation introduced by the numerical scheme. In this particular case, it corresponds to the dissipation of the first flexural mode of the plate, since it is the one predominantly excited. It can be seen that, as the mesh is refined, the dissipation is clearly reduced. The results of the $2\text{x}(100\text{x}25)$ mesh compare well against the solution provided in [9]. Finally, Figure 11 shows the evolution in time of the vertical displacement and vertical velocity at $\mathbf{X} = (0, 0)^T$. It can be seen again the predominance of the first flexural mode, although as the mesh is refined higher modes emerge. Results compare well in terms of amplitude and frequency with the solution presented in [9].

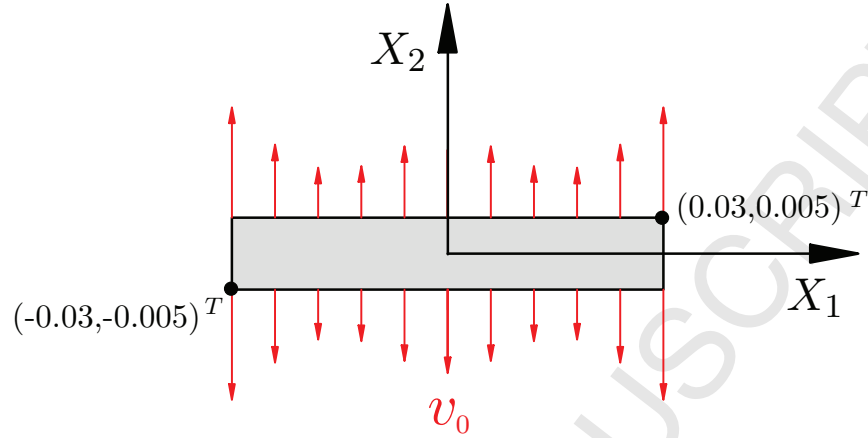


Figure 8: Beryllium plate initial configuration

7.3. Punch test

A squared two dimensional flat plate of unit side length is constrained to move tangentially on the east, west and south sides, whereas it is free on the north side (see Figure 12). The plate is subjected to an initial uniform velocity $v_{punch} = 100$ m/s on its right half side. The plate is composed of a neo-Hookean rubber material with Young's modulus $E = 1.7 \times 10^7$ Pa, density $\rho_0 = 1.1 \times 10^3$ Kg/m³ and Poisson's ratio $\nu = 0.45$. The problem shows the performance of the method with absence of volumetric locking and spurious modes (checker board) for the pressure.

Figure 13 compares results obtained using the Mean Dilatation technique and standard Finite Element Method (FEM) for the standard displacement based formulation against the JST algorithm using the proposed conservation mixed formulation. It can be seen how the standard FEM solution suffers from volumetric locking, while the Mean Dilatation technique is capable of circumventing it. However, both solutions exhibit spurious oscillations in the pressure field distribution. The JST alleviates both the volumetric locking and the appearance of the spurious pressure oscillations.

7.4. Bending column (2D)

A rubber-like column of 1 m width and 6 m height is clamped on its bottom end and subjected to an initial uniform horizontal velocity of $V_0 = 10$ m/s (see Figure 14). The example shows the performance of the numerical

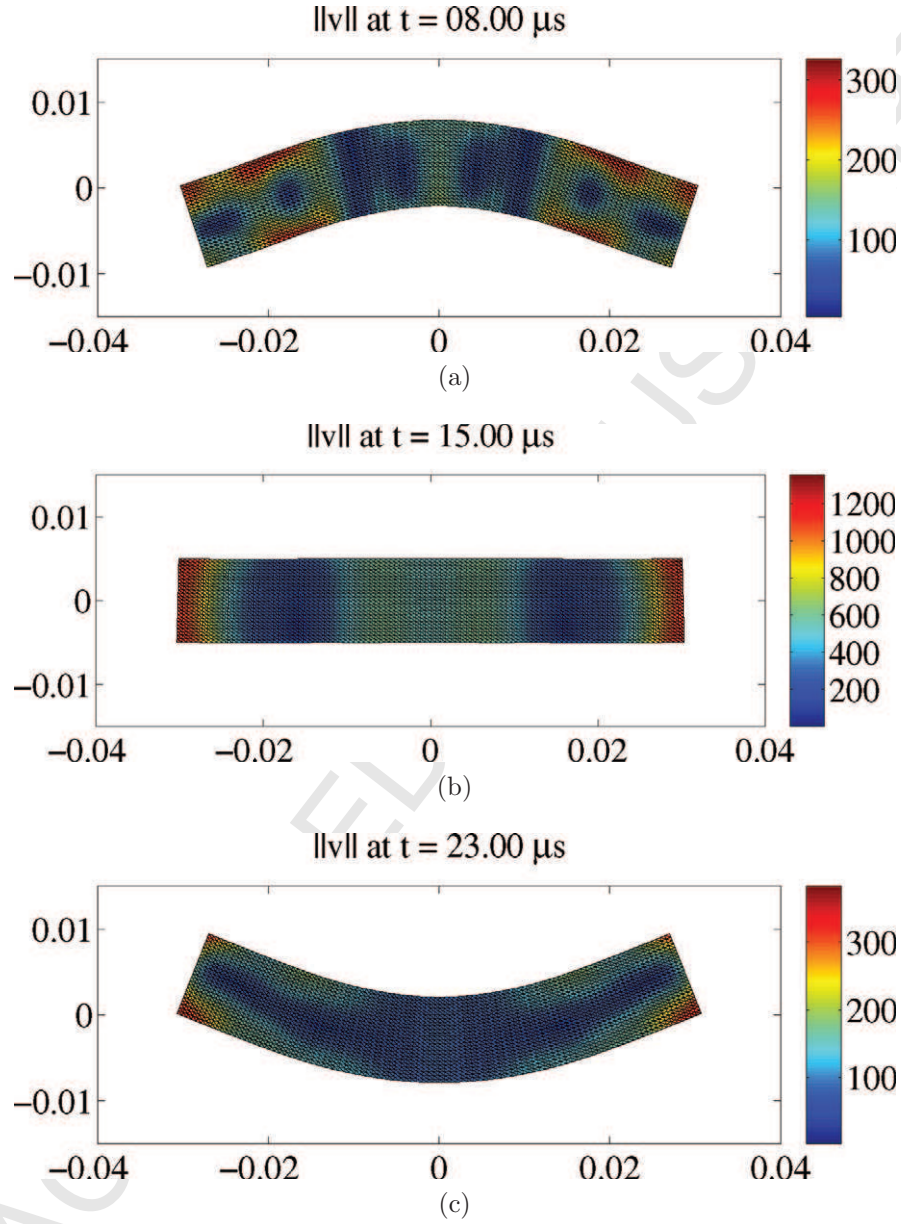


Figure 9: Beryllium plate. Material properties $\rho_0 = 1845 \text{ Kg/m}^3$, $E = 3.1827 \times 10^{11} \text{ Pa}$, $\nu = 0.05390$, $Y^0 = 1 \times 10^{11} \text{ Pa}$. Evolution in time of the deformed shaped. The contour plot represents the norm of the velocity vector. Solution obtained using $2 \times (100 \times 25)$ triangular elements and the JST method with $\kappa^{(4)} = 1/64$ and $\alpha_{CFL} = 0.4$.

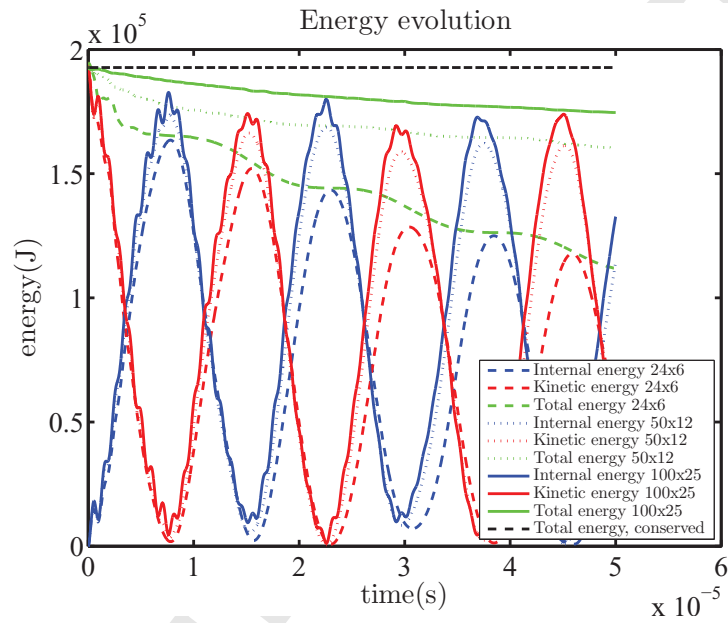


Figure 10: Beryllium plate. Material properties $\rho_0 = 1845 \text{ Kg/m}^3$, $E = 3.1827 \times 10^{11} \text{ Pa}$, $\nu = 0.05390\text{s}$, $Y^0 = 1 \times 10^{11} \text{ Pa}$. Evolution in time of the internal energy (blue lines), kinetic energy (red lines), summation of both (green lines) against the total conserved energy (black discontinuous line) for three different meshes of $2 \times (24 \times 6)$, $2 \times (50 \times 12)$ and $2 \times (100 \times 25)$ triangular elements. JST method with $\kappa^{(4)} = 1/64$ and $\alpha_{CFL} = 0.4$. The difference between the total conserved energy and the summation of internal and kinetic energy is the numerical dissipation.

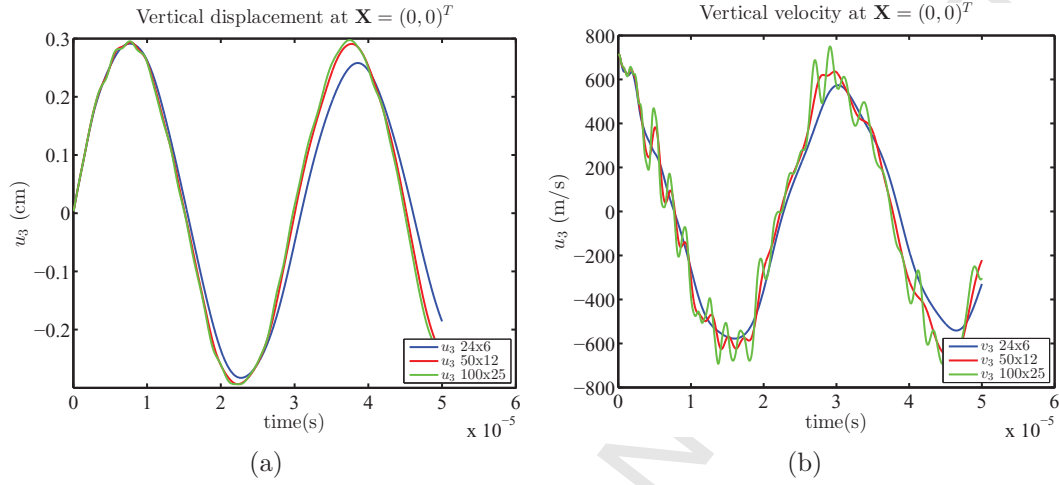


Figure 11: Beryllium plate. Material properties $\rho_0 = 1845 \text{ Kg/m}^3$, $E = 3.1827 \times 10^{11} \text{ Pa}$, $\nu = 0.05390\text{s}$, $Y^0 = 1 \times 10^{11} \text{ Pa}$. Evolution in time of the vertical displacement (a) and the vertical velocity (b) at $\mathbf{X} = (0,0)^T$ for three different meshes of $2 \times (24 \times 6)$, $2 \times (50 \times 12)$ and $2 \times (100 \times 25)$ triangular elements (blue, red and green lines, respectively). JST method with $\kappa^{(4)} = 1/64$ and $\alpha_{CFL} = 0.4$.

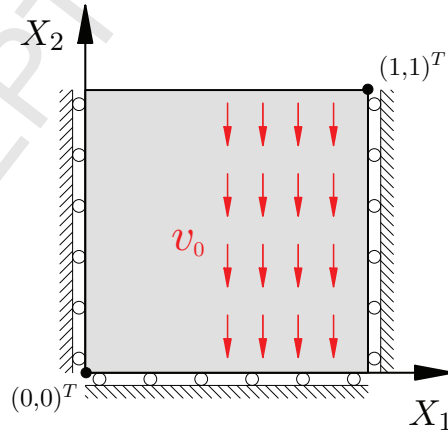


Figure 12: Punch test case initial configuration

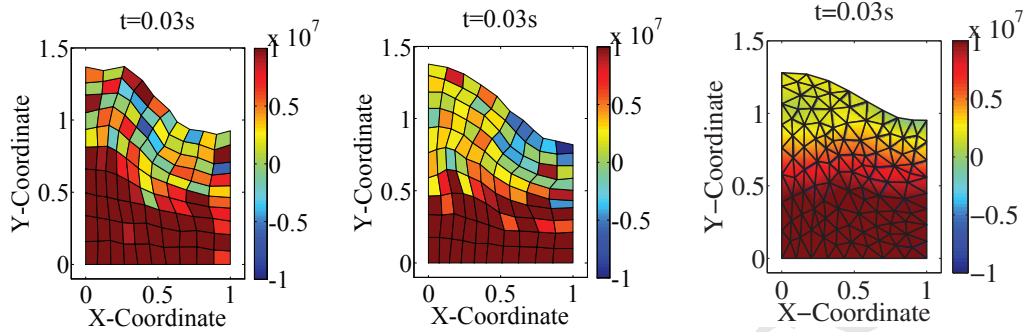


Figure 13: Numerical solution of the punch test case with an initial uniform velocity at the right hand side $v_{punch} = 100$ m/s. Material properties $E = 1.7 \times 10^7$ Pa, $\rho_0 = 1.1 \times 10^3$ Kg/m³, $\nu = 0.45$ for a neo-Hookean material. The solution is shown at time $t = 0.03$ s for different discretisations. From left to right: FEM displacement based, Mean dilatation, and JST. All the solutions have been obtained using a discretisation of 121 nodes.

technique in bending dominated scenarios. The material is chosen as neo-Hookean with Young's modulus $E = 1.7 \times 10^7$ Pa, density $\rho_0 = 1.1 \times 10^3$ Kg/m³ and Poisson's ratio $\nu = 0.45$. Figure 15 shows the JST solution (column (c)) at different times as compared to the PG solution (column (b)) and the cell centred Finite Volume solution (column (a)). The same mesh of 8×48 quadrilateral elements ($\Delta x_{max} = 0.125$ m) was employed for comparison purposes. All three solutions exhibit very similar deformation patterns with smooth pressure distribution and absence of locking. Comparison of the resolution of the three solutions shows that the JST method offers the most dissipative solution, whereas the PG method provides the most accurate solution (but at a greater computational cost).

Figure 16 presents the results for the JST method using a more refined unstructured mesh with $\Delta x_{max} = 0.05$ m, which naturally leads to more accurate results.

7.5. Collapse of a thick-walled cylindrical beryllium shell

This test problem was initially proposed by [13] and later implemented in [14] and [15] in order to assess the ability of a computational method to model plastic flows. A thick-walled cylindrical beryllium shell has an initial radial

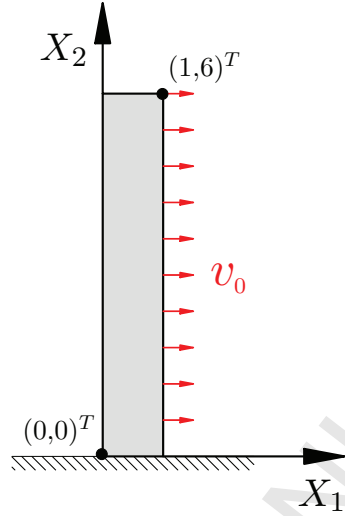


Figure 14: Bending column initial configuration

velocity directed towards its centre. Plane strain conditions are assumed for the shell. After a certain time, all the kinetic energy of the material should be transformed into plastic dissipation. The final interior and exterior radii of the shell are called stopping radii, and a closed form solution for both was provided in [13]. In this paper, the problem presented in [15] will be modelled.

The shell is centred at $\mathbf{X} = (0,0)^T$ m and has an initial interior radius $R_i = 80 \cdot 10^{-3}$ m and an outer radius $R_o = 100 \cdot 10^{-3}$ m. The material is modelled using a hyperelastic-plastic constitutive model (see algorithm 2.1) and a Mie-Gruneisen equation of state (see equation (16)). The material parameters are $\rho_0 = 1845$ Kg/m³, $\Gamma_0 = 2$, $c_0 = 12870$ m/s and $s = 1.124$. The elastic-plastic constitutive law is characterized by the shear modulus $\mu = 151.9 \times 10^9$ Pa, yield strength $Y^0 = 330 \times 10^6$ Pa and hardening modulus $H = 0$ Pa (perfectly plastic material). The initial velocity field is defined by

$$\mathbf{v}(\mathbf{X}, t_0) = -V_0 \frac{R_i}{\|X_1^2 + X_2^2\|^2} (X_1, X_2)^T \quad \text{m/s}$$

and the exterior pressure is defined as $p = 1 \times 10^{-6}$ Pa. The shell is simulated using relevant boundary conditions. A mesh of $2 \times (20 \times 8)$ triangular elements

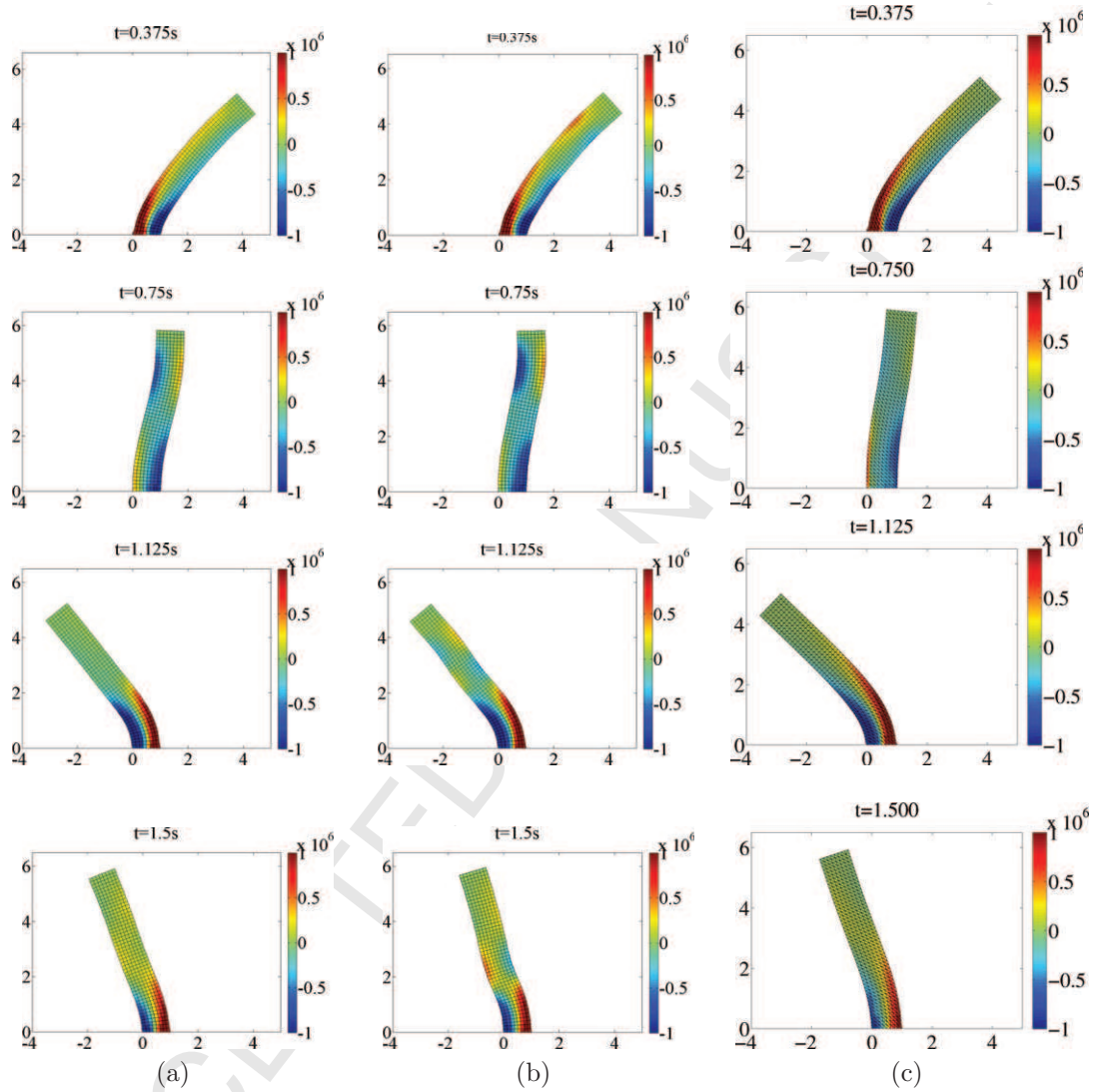


Figure 15: Bending column: Sequence of pressure distribution of deformed shapes using: column (a) CCFVM imposing piecewise linear reconstruction (see reference [1]); column (b) PG (consistent mass, $\tau_F = \Delta t$, $\tau_p = 0$, $\alpha = 0.05$) (see reference [2]) and column (c) JST ($\kappa^{(4)} = 1/64$). Results obtained with initial horizontal velocity $V_0 = 10\text{m/s}$. The nearly incompressible neo-Hookean constitutive model is used with Poisson's ratio $\nu = 0.45$, Young's modulus $E = 1.7 \times 10^7\text{Pa}$, density $\rho_0 = 1.1 \times 10^3\text{kg/m}^3$ and $\alpha_{CFL} \approx 0.4$. Discretisation with 8×48 quadrilateral elements with $\Delta x_{max} = 0.125\text{ m}$. Time step $\Delta t = 1 \times 10^{-4}\text{s}$.

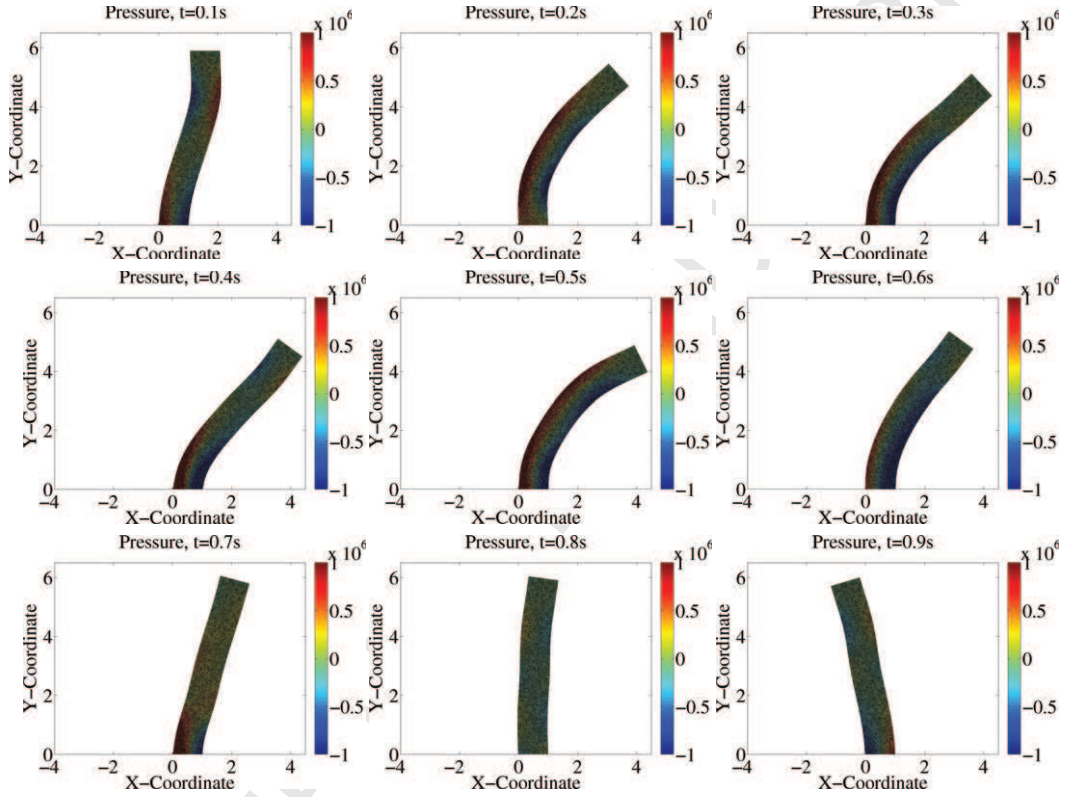


Figure 16: Bending column. Results obtained with initial horizontal velocity $V_0 = 10\text{m/s}$. The nearly incompressible neo-Hookean constitutive model is used with Poisson's ratio $\nu = 0.45$, Young's modulus $E = 1.7 \times 10^7\text{Pa}$, density $\rho_0 = 1.1 \times 10^3\text{kg/m}^3$ and $\alpha_{CFL} \approx 0.4$. Discretisation using the JST method with an unstructured mesh and $\kappa^{(4)} = 1/64$, $\Delta t = 2.5 \times 10^{-5}$, $\Delta x_{max} = 0.05\text{m}$.

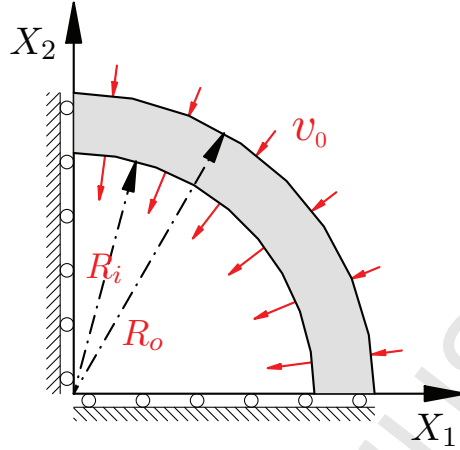


Figure 17: Beryllium shell initial configuration

is used, which has 720 degrees of freedom. The dissipation parameter is set to $\kappa^{(4)} = 1/1024$.

In [13], a closed form solution at the stopping time was obtained considering an incompressible material and that all the energy of the system is dissipated through plasticity. This yields a relationship between the initial velocity \mathbf{v}_0 and the inner and outer stopping radii. As in [13], the simulation has been performed for three different initial velocities $\mathbf{v}_0 = 417.1$ m/s, $\mathbf{v}_0 = 454.7$ m/s and $\mathbf{v}_0 = 490.2$ m/s, and the analytical results, as presented in Table 1, are used for the benchmarking the problem.

Figure 18 shows the results for the three cases at the stopping time, where the plastic strain (left) and the initial and final meshes (right) are depicted. The final mesh is compared against the analytical solution. It is confirmed the good axisymmetry of the three solutions. In Table 2, the inner and outer stopping radii are compared against the analytical solution. It transpires that there is a match against the analytical solution, where the maximum error is 0.135 %. The table also shows the stopping time of the solutions. All results are in good agreement with those provided in [13], despite using a much coarser mesh in this paper.

Next, the axisymmetry of the solutions is quantified as in [13]. Firstly, the mean radius of the 9 different circumferential rings of the mesh is computed as \bar{R}^i , $i = \{1, \dots, 9\}$. Next, the radius deviation is computed per node, com-

Table 1: Analytical results for the Beryllium shell problem [13]

v_0 (m/s)	Outer stopping radius (mm)	Inner stopping radius (mm)
417.1	50	78.10
454.7	45	75.00
490.2	40	72.12

Table 2: Numerical results for the Beryllium shell problem. Table shows the stopping time, and the error in the inner and outer radius for the three different solutions

Stopping radius (mm)	Stopping time (ms)	Inner radius error (%)	Outer radius error (%)
50	125.6	+0.135	+0.022
45	131.6	+0.106	-0.012
40	136.2	+0.030	-0.072

paring the nodal radius against the mean radius of its corresponding layer. This information is used as well for computing the standard deviation. Table 3 shows the obtained results. It can be seen how the algorithm is capable of preserving an excellent axisymmetry, giving maximum standard deviation of the order 10^{-9} .

Finally, in Figure 19, the evolution of the inner and outer radii is shown and compared against the analytical solution. This shows a good convergence of both three results as the shell reaches its stopping time.

7.6. L-shaped block

This example was first proposed by Simo et al. in [63] and later implemented by several authors (see for example references [64–66]). In what follows, the results for the example as proposed in [66] for a neo-Hookean material will be shown. A three-dimensional L-shaped block is left free in space and subjected to time varying forces at two of its sides (see Figure 20). These forces are described by the equations,

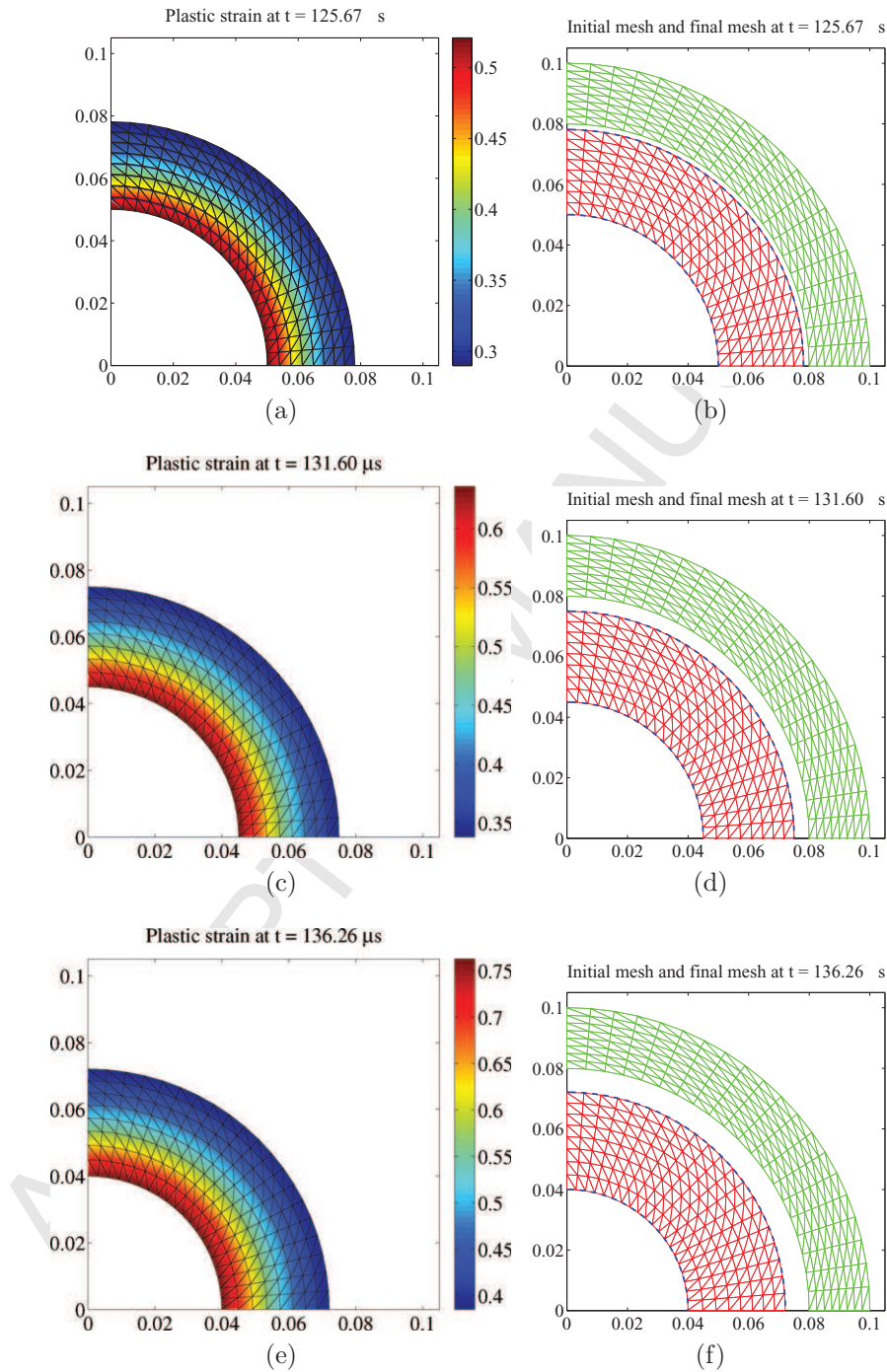


Figure 18: Beryllium shell problem. Hyperelastic-plastic constitutive model and Mie-Gruneisen equation of state. Material parameters: $\rho_0 = 1845 \text{ Kg/m}^3$, $\Gamma_0 = 2$, $c_0 = 12870 \text{ m/s}$, $\mu = 151.9 \times 10^9 \text{ Pa}$, $Y^0 = 330 \times 10^6 \text{ Pa}$, $H = 0 \text{ Pa}$. Mesh of $2 \times (40 \times 32)$ triangular elements and 1353 degrees of freedom. Dissipation parameter $\kappa^{(4)} = 1/2048$. From top to bottom rows, results are shown for initial velocities $\mathbf{v}_0 = 417.1 \text{ m/s}$, $\mathbf{v}_0 = 454.7 \text{ m/s}$ and $\mathbf{v}_0 = 490.2 \text{ m/s}$ at their stopping time. Plastic strain is shown in the left column. Initial mesh (green) and final mesh (red) against

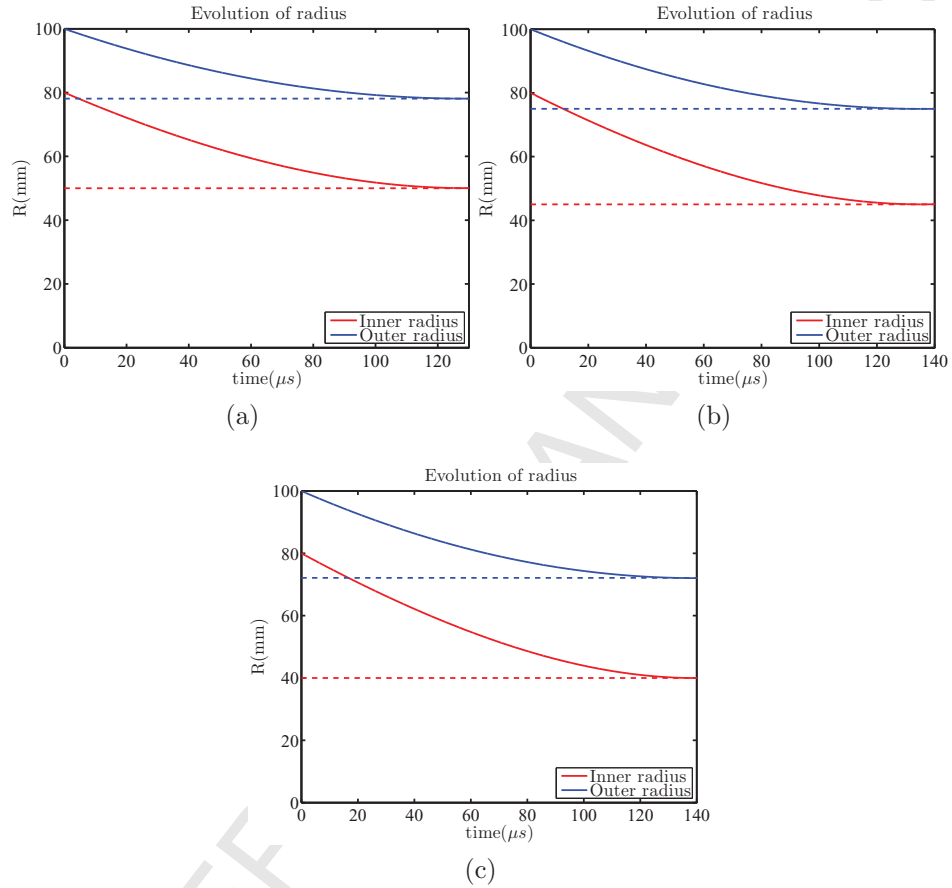


Figure 19: Beryllium shell problem. Hyperelastic-plastic constitutive model and Mie-Gruneisen equation of state. Material parameters: $\rho_0 = 1845$ Kg/m³, $\Gamma_0 = 2$, $c_0 = 12870$ m/s, $s = 1.124$, $\mu = 151.9 \times 10^9$ Pa, $Y^0 = 330 \times 10^6$ Pa, $H = 0$ Pa. Mesh of $2 \times (40 \times 32)$ triangular elements and 1353 degrees of freedom. Dissipation parameter $\kappa^{(4)} = 1/2048$. The evolution of the radius is shown for the three test cases: $v_0 = 417.1$ m/s (a), $v_0 = 454.7$ m/s (b) and $v_0 = 490.2$ m/s (c). The inner radius (continuous thick red line) and the outer radius (continuous thick blue line) are compared against the analytical solution (discontinuous lines).

Table 3: Numerical results for the Beryllium shell problem. The table shows the standard deviation of the radius for each of the layers of the mesh. The minimum and maximum deviation among all the nodes is as well presented.

Stopping radius (mm)	Standard deviation σ (%)	Minimum deviation (%)	Maximum deviation (%)
50	$6.74 \cdot 10^{-10}$	$-2.61 \cdot 10^{-11}$	$+2.98 \cdot 10^{-11}$
45	$9.84 \cdot 10^{-10}$	$-5.10 \cdot 10^{-11}$	$4.12 \cdot 10^{-11}$
40	$1.62 \cdot 10^{-9}$	$-9.00 \cdot 10^{-11}$	$+7.98 \cdot 10^{-11}$

$$\mathbf{F}_1(t) = -\mathbf{F}_2(t) = (150, 300, 450)p(t), \quad p(t) = \begin{cases} t, & 0 \leq t < 2.5, \\ 5 - t, & 2.5 \leq t < 5, \\ 0, & t \geq 5. \end{cases}$$

The block is made of a neo-Hookean material, with properties $\mu = 1.925 \times 10^4$ Pa, $\lambda = 2.885 \times 10^4$ Pa and $\rho_0 = 1.0 \times 10^3$ kg/m³. Figure 21 shows the evolution in time of the pressure and deformed shape. Figure 22a demonstrates the ability of the algorithm to preserve the angular momentum (once the external forces are released) and linear momentum (the external torque is applied at the centre of mass of the block). Figure 22b compares the total energy of the system (red line) and the summation of kinetic and potential energies (blue lines) when using three different tetrahedral meshes: 388, 1178 and 3546 nodes. It can be seen that, as the mesh is refined, the numerical dissipation (difference between the total energy of the system and the summation of kinetic and potential energies) is reduced, obtaining therefore a more accurate solution.

7.7. Bending column (3D)

This example is an extension of the two-dimensional column presented previously. The problem is shown to demonstrate the performance of the method in three-dimensional bending dominated scenarios. As in the two-dimensional case, a rubber-like material column is clamped on its bottom face ($X_3 = 0$ m). An initial uniform velocity $\mathbf{V}_0 = 10 \left(\frac{\sqrt{3}}{2}, \frac{1}{2}, 0 \right)^T$ m/s is

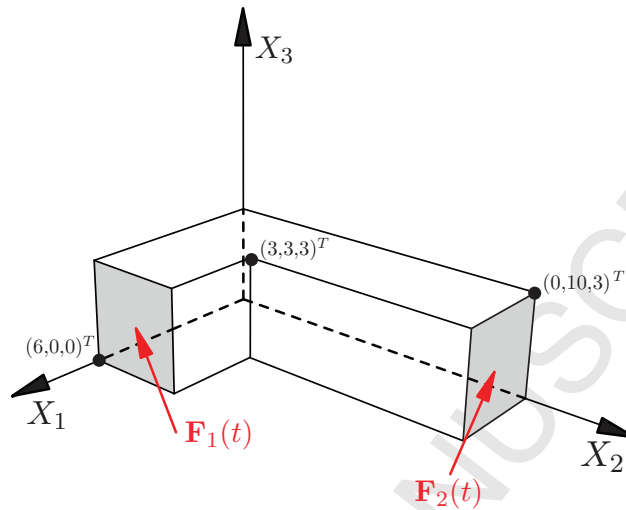


Figure 20: L-shaped block, initial configuration

imposed and the bar is left oscillating freely in time (see Figure 23). A neo-Hookean material is chosen with Young's modulus $E = 1.7 \times 10^7$ Pa, density $\rho_0 = 1.1 \times 10^3$ Kg/m³ and Poisson's ratio $\nu = 0.45$.

Figure 24 shows the evolution in time of the pressure distribution for the deformed configuration. The solution exhibits a smooth distribution of pressure and absence of locking. In addition, figure 25 shows the time history of the vertical displacement (X_3 direction) at point $\mathbf{X} = (1, 1, 6)^T$ m and stress component P_{33} history at point $\mathbf{X} = (0, 0, 0)^T$ for three different spatial discretisations, $h = 1/3$ m, $h = 1/6$ m and $h = 1/12$ m. These figures illustrate the convergence of the solution as the mesh is refined.

Next, the example is extended to show the performance of the method when plasticity is involved. Figure 26 compares at time step $t = 0.45$ s the previous neo-Hookean solution against two solutions using Von-Mises hyperelastic-plastic material with yield stress $\bar{\tau}_y^0 = 2$ GPa and yield stress $\bar{\tau}_y^0 = 1$ GPa, respectively, and isotropic hardening modulus $H = 0.5$ GPa (the rest of the material parameters are the same as those of the previous neo-Hookean example for the three simulated cases). As can be observed, the pressure distribution is smooth and the occurrence of plasticity is perfectly depicted in the clamped end of the column. As expected, the column with lowest yield stress shows a higher deflection.

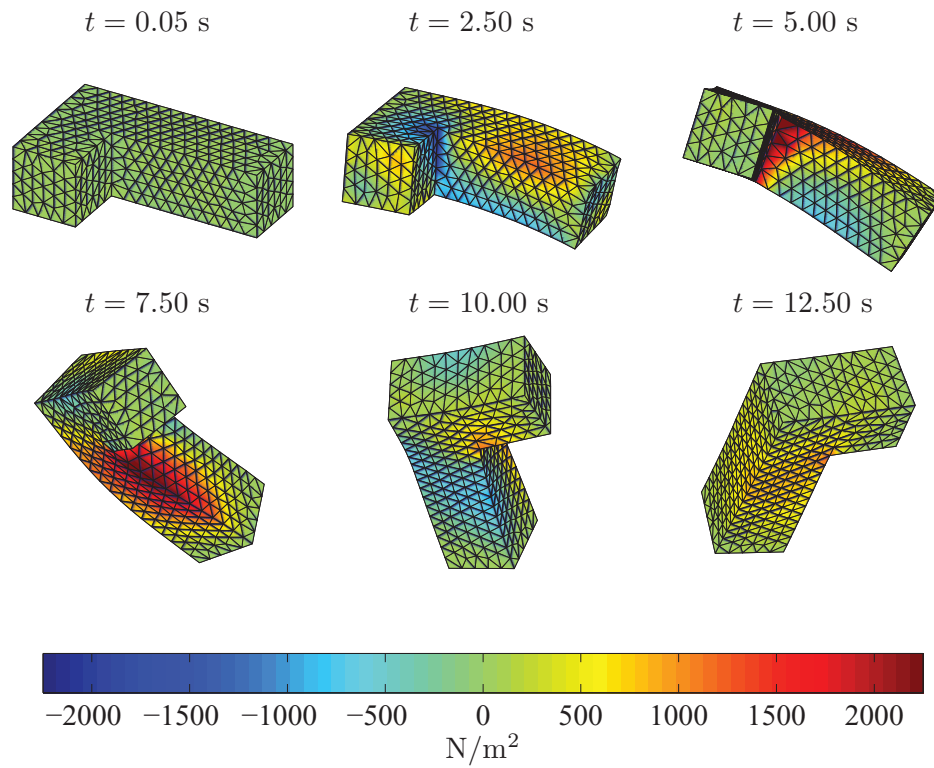


Figure 21: L-shaped block, evolution in time of deformation and pressure distribution. Neo-Hookean material with material properties $\mu = 1.925 \times 10^4$ Pa, $\lambda = 2.885 \times 10^4$ Pa, $\rho_0 = 1.0 \times 10^3 \text{kg/m}^3$. JST spatial discretisation using a tetrahedral mesh of 1178 nodes, $\kappa^{(4)} = 1/128$ and $\alpha_{CFL} = 0.4$.

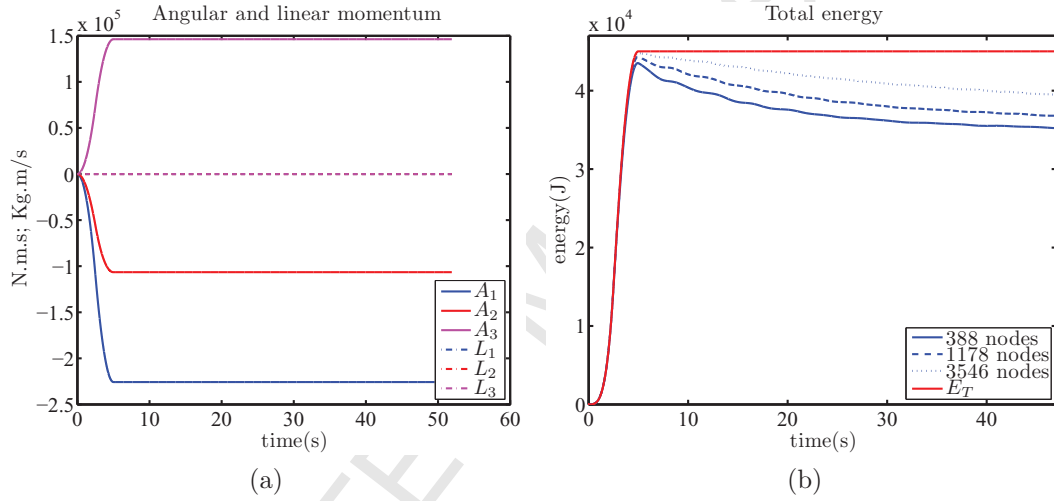


Figure 22: L-shaped block neo-Hookean material with material properties $\mu = 1.925 \times 10^4$ Pa, $\lambda = 2.885 \times 10^4$ Pa, $\rho_0 = 1.0 \times 10^3$ kg/m³. JST spatial discretisation using $\kappa^{(4)} = 1/128$ and $\alpha_{CFL} = 0.4$. (a) Conservation of linear momentum $\mathbf{p} = [L_1, L_2, L_3]^T$ and angular momentum $\mathbf{A} = [A_1, A_2, A_3]^T$ for a mesh of 1178 nodes; (b) comparison on the preservation of the total energy when using three different tetrahedral meshes: 388, 1178 and 3546 nodes.

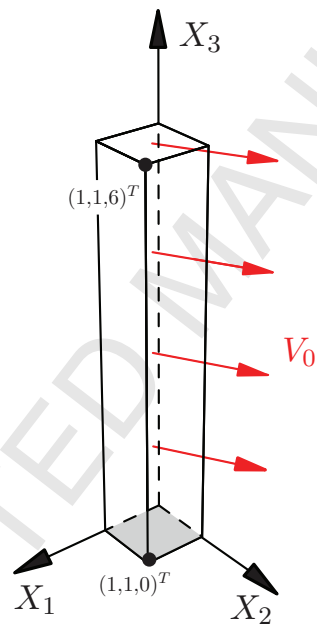


Figure 23: Three dimensional bending column. Initial configuration.

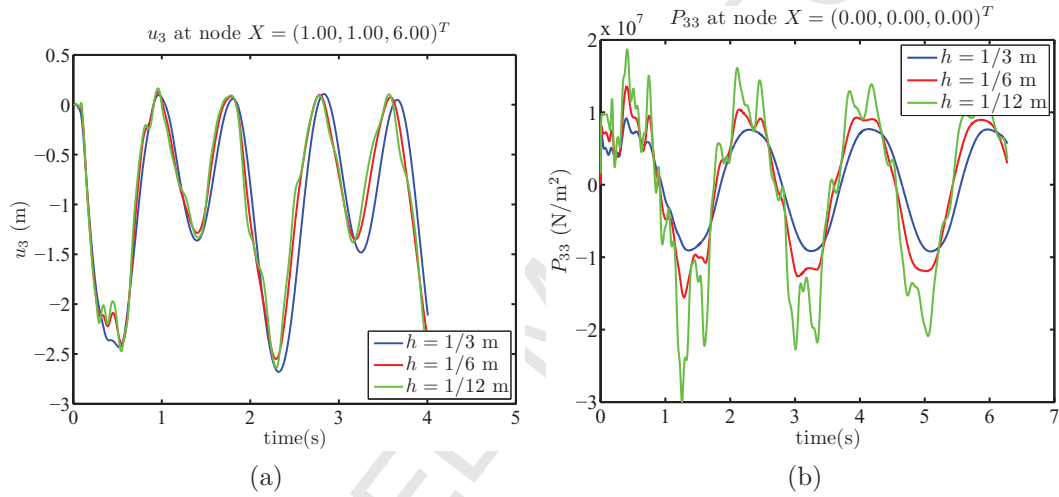


Figure 25: Three dimensional bending column. (a) Time history of the vertical displacement at node $\mathbf{X} = (1, 1, 6)^T$ m; (b) time history of the stress P_{33} at node $\mathbf{X} = (1/3, 1/3, 3)^T$ m. Initial uniform velocity $\mathbf{V}_0 = 10 \left(\frac{\sqrt{3}}{2}, \frac{1}{2}, 0 \right)^T$ m/s. NeoHookean material with Young's modulus $E = 1.7 \times 10^7$ Pa, density $\rho_0 = 1.1 \times 10^3$ Kg/m³ and Poisson's ratio $\nu = 0.45$. JST spatial discretisation with $h = 1/3$ m (blue), $h = 1/6$ m (red) and $h = 1/12$ m (green), $\kappa^{(4)} = 1/128$ and $\alpha_{CFL} = 0.4$.

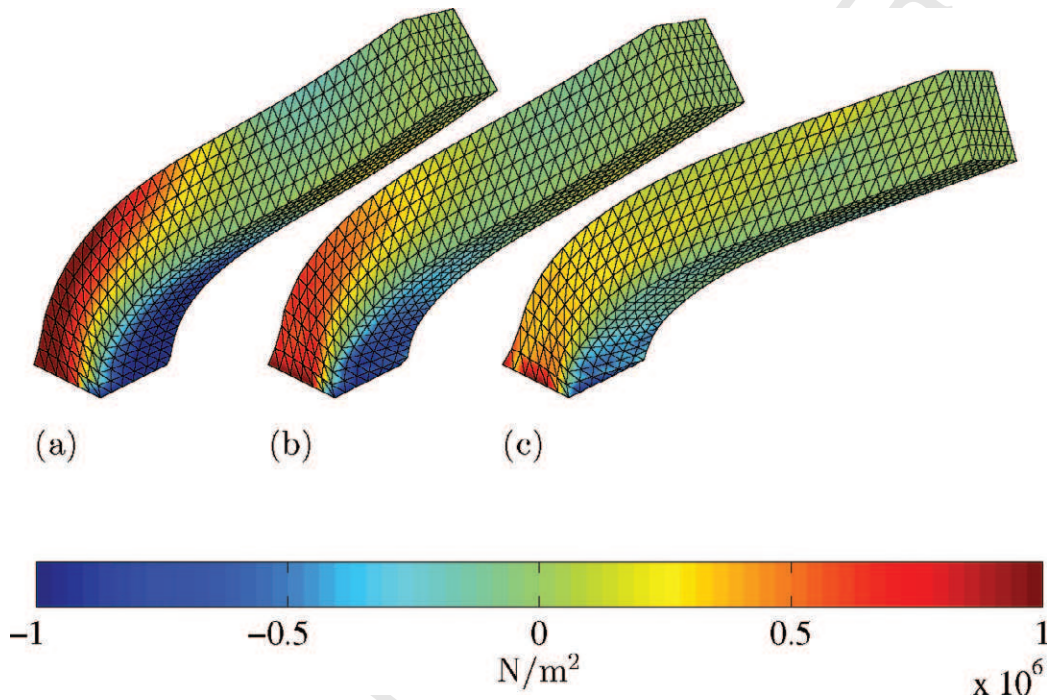


Figure 26: Three dimensional bending column. Initial uniform velocity $\mathbf{V}_0 = 10(\cos(30), \sin(30), 0)^T$ m/s. Comparison of the pressure distribution for two different materials: hyperelastic constitutive model (a), Von-Mises hyperelastic plastic constitutive models (b), (c) at time $t = 0.45$ s. Young's modulus $E = 1.7 \times 10^7 \text{ Pa}$, density $\rho_0 = 1.1 \times 10^3 \text{ Kg/m}^3$ and Poisson's ratio $\nu = 0.45$. Yield stress, $\bar{\tau}_y^0 = 2 \text{ GPa}$ (b), $\bar{\tau}_y^0 = 1 \text{ GPa}$ (c), hardening modulus $H = 0.5 \text{ GPa}$. JST spatial discretisation with $h = 1/6 \text{ m}$, $\kappa^{(4)} = 1/128$ and $\alpha_{CFL} = 0.4$.

Table 4: Taylor test. Final radius at $t = 80\mu\text{s}$ of the proposed method compared to other methodologies and experimental results

Method	final radius (mm)
FEM tetrahedrals	5.55
FEM hexahedras	6.95
FEM average nodal pressure	6.99
Proposed approach (JST)	6.98

7.8. Taylor impact case

A copper bar of initial length 0.0324 m and initial radius 0.0032 m has a velocity of 227 m/s and impacts against a rigid wall at time $t = 0$ s (see Figure 27). A Von-Mises hyperelastic-plastic material with isotropic hardening is chosen to simulate the material. The material parameters are Young's modulus $E = 117$ GPa, density $\rho_0 = 8.930 \times 10^3$ Kg/m³, Poisson's ratio $\nu = 0.35$, yield stress, $\bar{\tau}_y^0 = 0.4$ GPa and hardening modulus $H = 0.1$ GPa. Figure 28 shows the results obtained at four different time instants. The artificial dissipation can be reduced to $\kappa^{(4)} = 1/4096$ due to the presence of physical plastic dissipation in the material. The final radius at time $t = 80\mu\text{s}$ is shown in Table 4 as compared to numerical results using other methodologies [17], while experimental results can be found in [67]. As it is well known, the FEM solution with linear tetrahedrals suffer from volumetric locking, which is clearly seen in the results. The proposed formulation is able to circumvent this issue.

8. Conclusions

An adaptation of the Jameson-Schmidt-Turkel (JST) scheme for two-dimensional triangular and three-dimensional tetrahedral meshes has been implemented for a mixed conservation law in fast transient dynamics. The implementation has been specifically carried out in order to balance numerical stability, fulfilment of compatibility conditions and treatment of boundary conditions. This has resulted in an adapted JST scheme, where the numerical dissipation is only added to the equation of conservation of linear momentum and the boundary conditions are treated using an external loop on faces,

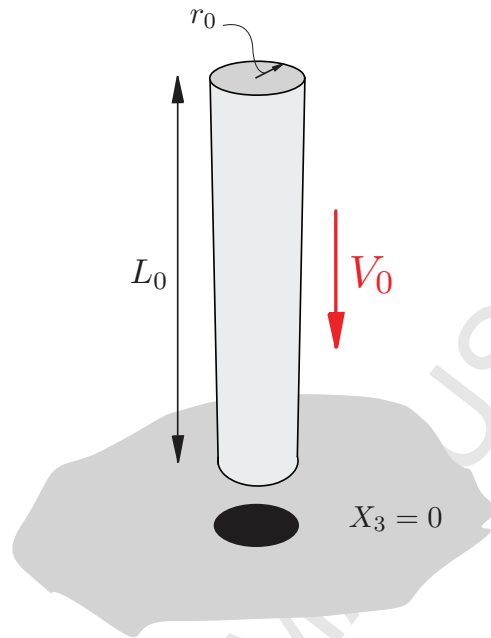


Figure 27: Setup of the Taylor test problem

where a weighted average of nodal flux evaluations ensures accuracy and robustness of the solution. In addition, the numerical algorithm is modified to ensure preservation of linear and angular momenta. Crucially, numerical results demonstrate second order convergence for both stresses and velocities, with excellent behaviour in bending dominated scenarios. Implementation of plasticity, or other constitutive models, proves to be straightforward. The obtained solutions compare well with other alternative methodologies, such as cell centred Finite Volume or stabilised Petrov Galerkin, previously published by the authors. Despite providing more dissipative solutions, the JST method constitutes an important alternative, as compared to other schemes, due to its computational efficiency.

The proposed methodology allows for further research including irreversible processes involving shocks, which can be dealt with through more complex constitutive models and the built-in shock capturing term. In addition, contact problems can as well be investigated by using alternative Riemann solvers on the external faces. A further improvement under investigation is the development of a time integration scheme which does not

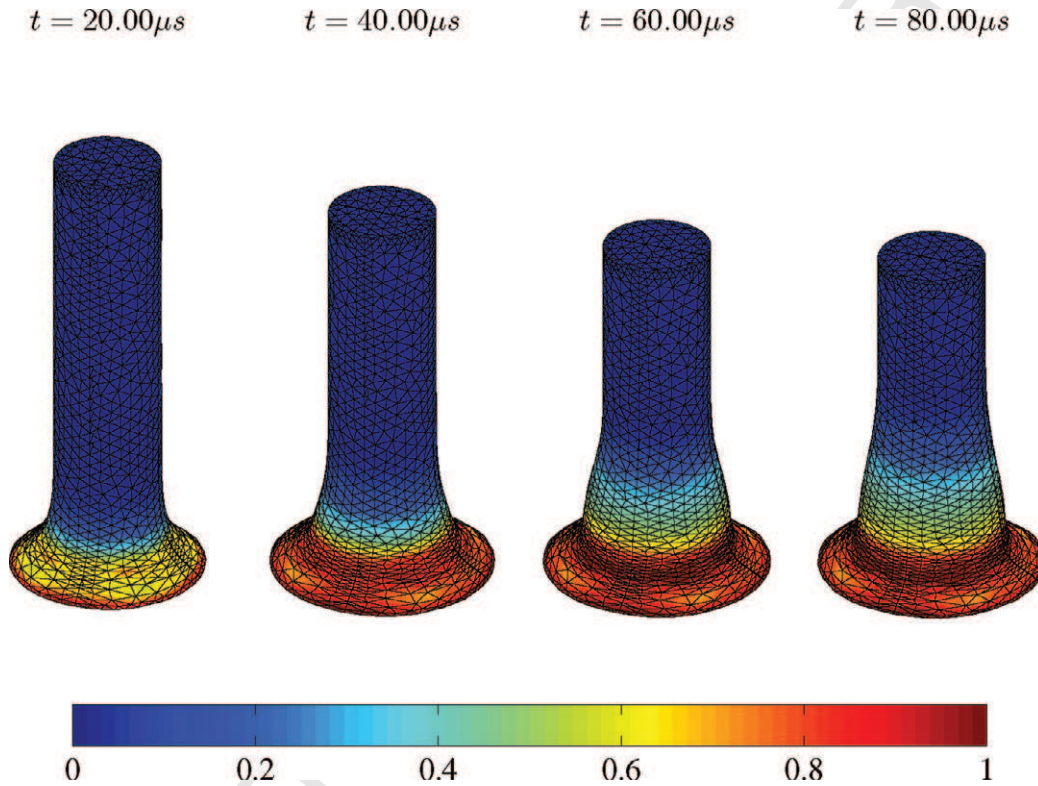


Figure 28: Taylor copper bar impact test. Initial velocity $v = 227$ m/s. Comparison of plastic strain at times $t = 20 \mu s$, $t = 40 \mu s$, $t = 60 \mu s$ and $t = 80 \mu s$. Young's modulus $E = 117$ GPa, density $\rho_0 = 8.930 \times 10^3$ Kg/m³, Poisson's ratio $\nu = 0.35$, Yield stress, $\bar{\tau}_y^0 = 0.4$ GPa and hardening modulus $H = 0.1$ GPa. JST spatial discretisation with 1361 nodes, $\kappa^{(4)} = 1/4096$ and $\alpha_{CFL} = 0.4$.

require the *a posteriori* correction of the interface tractions in order to satisfy conservation of angular momentum.

Acknowledgements

The authors acknowledge the financial support of the FP7 framework of the European Commission, through the Initial Training Network (ITN) Advanced Techniques in Computational Mechanics (ATCoMe), grant agreement 238548. The second author acknowledges the financial support received through “The Leverhulme Prize” awarded by The Leverhulme Trust, United Kingdom.

References

- [1] C. H. Lee, A. J. Gil, J. Bonet, Development of a cell centred upwind Finite Volume algorithm for a new conservation law formulation in structural dynamics, *Computers & Structures* 118 (2013) 13 – 38. Special Issue: UK Association for Computational Mechanics in Engineering.
- [2] C. H. Lee, A. J. Gil, J. Bonet, Development of a stabilised petrogalerkin formulation for conservation laws in lagrangian fast solid dynamics, *Computer Methods in Applied Mechanics and Engineering* 268 (2014) 40 – 64.
- [3] I. A. Karim, C. H. Lee, A. J. Gil, J. Bonet, A Two-Step Taylor Galerkin formulation for fast dynamics, *Engineering Computations* (2013). In Press.
- [4] N. Nguyen, J. Peraire, Hybridizable Discontinuous Galerkin Methods for partial differential equations in continuum mechanics, *Journal of Computational Physics* 231 (2012) 5955 – 5988.
- [5] Y. Fryer, C. Bailey, M. Cross, C.-H. Lai, A Control Volume procedure for solving the elastic stress-strain equations on an unstructured mesh, *Applied Mathematical Modelling* 15 (1991) 639 – 645.
- [6] C. Bailey, M. Cross, A Finite Volume procedure to solve elastic solid mechanics problems in three dimensions on an unstructured mesh, *International Journal for Numerical Methods in Engineering* 38 (1995) 1757–1776.
- [7] A. Slone, C. Bailey, M. Cross, Dynamic solid mechanics using Finite Volume Methods, *Applied Mathematical Modelling* 27 (2003) 69 – 87.

- [8] G. A. Taylor, C. Bailey, M. Cross, A vertex-based Finite Volume Method applied to non-linear material problems in computational solid mechanics, *International Journal for Numerical Methods in Engineering* 56 (2003) 507–529.
- [9] S. K. Sambasivan, M. J. Shashkov, D. E. Burton, A finite volume cell-centered lagrangian hydrodynamics approach for solids in general unstructured grids, *International Journal for Numerical Methods in Fluids* 72 (2013) 770–810.
- [10] J. A. Trangenstein, P. Colella, A higher-order godunov method for modeling finite deformation in elastic-plastic solids, *Communications on Pure and Applied Mathematics* 44 (1991) 41–100.
- [11] G. H. Miller, E. G. Puckett, A high-order godunov method for multiple condensed phases, *Journal of Computational Physics* 128 (1996) 134 – 164.
- [12] H. Tang, F. Sotiropoulos, A second-order godunov method for wave problems in coupled solid water gas systems, *Journal of Computational Physics* 151 (1999) 790 – 815.
- [13] B. P. Howell, G. J. Ball, A Free-Lagrange Augmented Godunov Method for the Simulation of Elastic-Plastic Solids, *Journal of Computational Physics* 175 (2002) 128 – 167.
- [14] G. Kluth, B. Després, Discretization of hyperelasticity on unstructured mesh with a cell-centered Lagrangian scheme, *Journal of Computational Physics* 229 (2010) 9092 – 9118.
- [15] P.-H. Maire, R. Abgrall, J. Breil, R. Loubère, B. Rebourec, A nominally second-order cell-centered Lagrangian scheme for simulating elastic-plastic flows on two-dimensional unstructured grids, *Journal of Computational Physics* 235 (2013) 626 – 665.
- [16] T. J. Hughes, *The Finite Element Method. Linear Static and Dynamic Finite Element Analysis*, Dover Publications, 2000.
- [17] J. Bonet, A. J. Burton, A simple average nodal pressure tetrahedral element for incompressible and nearly incompressible dynamic explicit

- applications, *Communications in Numerical Methods in Engineering* 14 (1998) 437–449.
- [18] J. Bonet, H. Marriott, O. Hassan, Stability and comparison of different linear tetrahedral formulations for nearly incompressible explicit dynamic applications, *International Journal for Numerical Methods in Engineering* 50 (2001) 119–133.
- [19] J. Bonet, H. Marriott, O. Hassan, An averaged nodal deformation gradient linear tetrahedral element for large strain explicit dynamic applications, *Communications in Numerical Methods in Engineering* 17 (2001) 551–561.
- [20] S. K. Lahiri, J. Bonet, J. Peraire, L. Casals, A variationally consistent fractional time-step integration method for incompressible and nearly incompressible lagrangian dynamics, *International Journal for Numerical Methods in Engineering* 63 (2005) 1371–1395.
- [21] S. K. Lahiri, J. Bonet, J. Peraire, A variationally consistent mesh adaptation method for triangular elements in explicit Lagrangian dynamics, *International Journal for Numerical Methods in Engineering* 82 (2010) 1073–1113.
- [22] C. Dohrmann, M. W. Heinstein, J. Jung, S. W. Key, W. R. Witkowski, Node-based uniform strain elements for three-node triangular and four-node tetrahedral meshes, *International Journal for Numerical Methods in Engineering* 47 (2000) 1549–1568.
- [23] G. Scovazzi, Stabilized shock Hydrodynamics: II. Design and physical interpretation of the SUPG operator for Lagrangian computations, *Computer Methods in Applied Mechanics and Engineering* 196 (2007) 967 – 978.
- [24] G. Scovazzi, M. Christon, T. Hughes, J. Shadid, Stabilized shock Hydrodynamics: I. a Lagrangian method, *Computer Methods in Applied Mechanics and Engineering* 196 (2007) 923 – 966.
- [25] G. Scovazzi, E. Love, M. Shashkov, Multi-scale Lagrangian shock Hydrodynamics on Q1/P0 finite elements: Theoretical framework and two-dimensional computations, *Computer Methods in Applied Mechanics and Engineering* 197 (2008) 1056 – 1079.

- [26] G. Scovazzi, J. Shadid, E. Love, W. Rider, A conservative nodal Variational Multiscale Method for Lagrangian shock Hydrodynamics, *Computer Methods in Applied Mechanics and Engineering* 199 (2010) 3059 – 3100.
- [27] G. Scovazzi, Lagrangian shock Hydrodynamics on tetrahedral meshes: A stable and accurate Variational Multiscale approach, *Journal of Computational Physics* 231 (2012) 8029 – 8069.
- [28] R. J. Leveque, *Finite-Volume Methods for Hyperbolic Problems*, Cambridge University Press, 2004.
- [29] E. F. Toro, *Riemann Solvers and Numerical Methods for Fluid Dynamics*, Springer, 1999.
- [30] H. Versteeg, W. Malalasekera, *An Introduction to Computational Fluid Dynamics. The Finite Volume Method*, Pearson/Prentice Hall, 2007.
- [31] T. Hughes, L. Franca, M. Mallet, A new Finite Element formulation for computational fluid dynamics: I. Symmetric forms of the compressible Euler and Navier-Stokes equations and the second law of thermodynamics, *Computer Methods in Applied Mechanics and Engineering* 54 (1986) 223 – 234.
- [32] T. J. Hughes, Multiscale phenomena: Green’s functions, the Dirichlet-to-Neumann formulation, subgrid scale models, bubbles and the origins of stabilized methods, *Computer Methods in Applied Mechanics and Engineering* 127 (1995) 387 – 401.
- [33] A. Jameson, W. Schmidt, E. Turkel, Numerical solution of the Euler equations by Finite Volume methods using Runge-Kutta time-stepping schemes, *AIAA 5th Computational Fluid Dynamics Conference* 81 (1981) 1259.
- [34] A. Jameson, T. Baker, N. P. Weatherill, Calculation of inviscid transonic flow over a complete aircraft, *AIAA 24th Aerospace Sciences Meeting* (1986).
- [35] D. Mavriplis, Multigrid solution of the Navier-Stokes equations on triangular meshes, *AIAA Journal* 26 (1989) 824–831.

- [36] R. Rausch, J. Batina, H. Yang, Spatial adaption procedures on unstructured meshes for accurate unsteady aerodynamic flow computations, AIAA Paper 91-1106 (1991).
- [37] N. Frink, Recent progress toward a three-dimensional Navier-Stokes solver, in: AIAA Paper 94-0061.
- [38] T. Barth, On unstructured grids and solvers, VKI, Computational Fluid Dynamics, Volume 2 66 p (SEE N90-27993 22-34) 2 (1990).
- [39] D. J. Mavriplis, Unstructured grid techniques, Annual Review of Fluid Mechanics 29 (1997) 473–514.
- [40] K. Morgan, J. Peraire, Unstructured grid Finite-Element methods for fluid mechanics, Reports on Progress in Physics 61 (1998) 569–638.
- [41] C. Hirsch, Numerical Computation of Internal & External Flows. Volume 1: Fundamentals of Computational Fluid Dynamics, volume 1, Elsevier, 2007 edition, 2007.
- [42] R. C. Swanson, E. Turkel, On central-difference and upwind schemes, Journal of Computational Physics 101 (1992) 292 – 306.
- [43] P. Jorgenson, E. Turkel, Central difference TVD schemes for time dependent and steady state problems, Journal of Computational Physics 107 (1993) 297 – 308.
- [44] K. A. Sørensen, O. Hassan, K. Morgan, N. P. Weatherill, A multi-grid accelerated hybrid unstructured mesh method for 3D compressible turbulent flow, Computational Mechanics 31 (2003) 101–114.
- [45] J. Blazek, Computational fluid dynamics: principles and applications, Elsevier, 2nd edition, 2005.
- [46] T. Barth, Aspects of unstructured grids and Finite-Volume solvers for the Euler and Navier-Stokes equations, AGARD R-787, Special Course on Unstructured Grid Methods for Advection Dominated Flows, Brussels, Belgium (1992) 6.1–6.61.
- [47] F. Johnson, E. Tinoco, N. Yu, Thirty years of development and application of CFD at Boeing commercial airplanes, Seattle, AIAA Computational Fluid Dynamics Conference (2003).

- [48] B. Courbet, C. Benoit, V. Couaillier, F. Haider, M. Le Pape, S. Péron, Space discretization methods, *Aerospace Lab Journal* (2011).
- [49] C.-W. Shu, S. Osher, Efficient implementation of essentially non-oscillatory shock-capturing schemes, *Journal of Computational Physics* 77 (1988) 439 – 471.
- [50] C. H. Lee, Development of an Upwind Finite Volume Algorithm for a New Conservation Law Formulation in Structural Dynamics, Ph.D. thesis, Department of Civil Engineering. University of Wales. Swansea, 2011.
- [51] J. Marsden, T. Hughes, *Mathematical Foundations of Elasticity*, Dover Publications, 1983.
- [52] G. A. Holzapfel, *Nonlinear solid mechanics: a continuum approach for engineering*, Wiley, 2000.
- [53] J. Bonet, R. D. Wood, *Nonlinear Continuum Mechanics for Finite Element Analysis*, Cambridge University Press, 2nd edition, 2008.
- [54] J. Simo, Algorithms for static and dynamic multiplicative plasticity that preserve the classical return mapping schemes of the infinitesimal theory, *Computer Methods in Applied Mechanics and Engineering* 99 (1992) 61 – 112.
- [55] M. A. Meyers, *Dynamic behavior of materials*, John Wiley & Sons, Ltd, 1994.
- [56] H. Luo, J. Baum, R. Löhner, An improved Finite Volume scheme for compressible flows on unstructured grids, *AIAA paper* 95-0348 (1995).
- [57] A. Jameson, Solution of the Euler equations for two dimensional transonic flow by a multigrid method, *Applied Mathematics and Computation* 13 (1983) 327–355.
- [58] A. Jameson, Artificial diffusion, upwind biasing, limiters and their effect on accuracy and multigrid convergence in transonic and hypersonic flows, *AIAA Journal* . (1993) .

- [59] A. Jameson, Analysis and design of numerical schemes for gas dynamics, 1: artificial diffusion, upwind biasing, limiters and effect on accuracy and multigrid convergence, *International Journal of Computational Fluid Dynamics* 4 (1995) 171–218.
- [60] M. Torrilhon, Locally divergence-preserving upwind finite volume schemes for magnetohydrodynamic equations, *SIAM Journal on Scientific Computing* 26 (2005) 1166–1191.
- [61] B. Cockburn, C.-W. Shu, The Runge–Kutta Discontinuous Galerkin Method for Conservation Laws V: Multidimensional Systems, *Journal of Computational Physics* 141 (1998) 199 – 224.
- [62] S. Sambasivan, M. Shashkov, D. E. Burton, M. A. Christon, Mimetic theory for cell-centered Lagrangian finite volume formulation on general unstructured grids, Technical Report, Technical Report, Los Alamos National Laboratory, LAUR-12-231772012, Los Alamos National Laboratory (LANL), 2012.
- [63] J. Simo, N. Tarnow, The discrete energy-momentum method. Conserving algorithms for nonlinear elastodynamics, *Zeitschrift für angewandte Mathematik und Physik ZAMP* 43 (1992) 757–792.
- [64] X. Meng, T. Laursen, Energy consistent algorithms for dynamic finite deformation plasticity, *Computer Methods in Applied Mechanics and Engineering* 191 (2002) 1639 – 1675.
- [65] L. Noels, L. Stainier, J. P. Ponthot, An energy-momentum conserving algorithm for non-linear hypoelastic constitutive models, *International Journal for Numerical Methods in Engineering* 59 (2004) 83–114.
- [66] S. Dong, BDF-like methods for nonlinear dynamic analysis, *Journal of Computational Physics* 229 (2010) 3019 – 3045.
- [67] M. L. Wilkins, M. W. Guinan, Impact of cylinders on a rigid boundary, *Journal of Applied Physics* 44 (1973) 1200–1206.